ApoE ε4 allele showed extensive PiB uptake is consistent with these findings. Clinically diagnosed CBD or CBS [39] encompasses various kinds of neurodegenerative diseases, such as AD, progressive supranuclear palsy, and Pick's disease [40]. The findings in our patient suggest that the asymmetric deposition of Aβ in the striatum and primary sensorimotor cortex can give rise to atypical AD that mimics CBD.

It should be noted that the patient had stenosis of the right middle cerebral artery and right fetal type posterior cerebral artery originating from the internal cerebral artery. It is conceivable that persistent hypoperfusion of the right middle cerebral artery led to Aβ deposition that was more pronounced on the right.

As described in "Introduction", there have been few reports on progressive apraxic agraphia. Our patient demonstrates that AD can present as progressive apraxic agraphia syndrome. Moreover, to the best of our knowledge, apraxic agraphia with micrographia has not been reported. Micrographia is typically observed in Parkinson's syndromes, such as Parkinson's disease, progressive supranuclear palsy [41], and CBD [39], but also occurs with focal damage to the putamen [42] or thalamus [43]. The combination of apraxic agraphia and micrographia suggests the involvement of the parietal cortex, basal ganglia, and thalamus, which was shown by PET and SPECT. It is known that extrapyramidal signs are uncommon in the early stage of AD, but are more prevalent as the disease progresses [44]. It should be noted that the basal ganglia and thalamus can be affected in the early stage of AD and cause parkinsonism.

Non-callosal ideomotor apraxia of the left hand

Ideomotor apraxia commonly manifests bilaterally. If ideomotor apraxia occurs unilaterally in the left hand, it is attributed to callosal disconnection [45]. As our patient did not exhibit any damage to the corpus callosum, the question remains as to why she showed unilateral ideomotor apraxia. Ideomotor apraxia of the left hand without a callosal lesion has already been reported in progressive apraxic agraphia [6]. Since transitive (using tools) action with the right hand was intact, the putative movement representations for skilled acts may have been preserved in the left parietal lobe. A problem occurs when stored movement information is transmitted to the right hemisphere through the corpus callosum. We assume that a "relative callosal disconnection" takes place when the right frontal and parietal lobes are functionally damaged and cannot properly process movement information transmitted from the left parietal lobe, as suggested by PET and SPECT. In any case, it should be noted that ideomotor apraxia of the left hand occurs without a callosal lesion, and this is possible only when there is hypometabolism or hypoperfusion in the right frontal and parietal lobes.

Further studies are needed to elucidate the spectrum of progressive apraxic agraphia and pathogenesis of non-callosal ideomotor apraxia of the left hand.

Acknowledgments The study was partly supported by a Grant-in-Aid for Comprehensive Research on Dementia (No 1103404) from the Ministry of Health, Labour, and Welfare of Japan (K.I.).

Conflicts of interest The authors declare that they have no conflict of interest.

References

1. Rapcsak SZ, Beeson PM (2002) Neuroanatomical correlates of spelling and writing. In: Hillis AE (ed) The handbook of adult language disorders. Integrating cognitive neuropsychology, neurology, and rehabilitation. Psychology Press, New York, pp 71–99
2. Ullrich L, Roeltgen DP (2011) Agraphia. In: Heilman KM, Valenstein E (eds) Clinical neuropsychology, 5th edn. Oxford University Press, New York, pp 130–151
3. Otsuki M, Soma Y, Arai T, Otsuka A, Tsuji S (1999) Pure apraxic agraphia with abnormal writing stroke sequences: report of a Japanese patient with a left superior parietal haemorrhage. J Neurol Neurosurg Psychiatry 66:233–237
4. Sakurai Y, Onuma Y, Nakazawa G, Ugawa Y, Momose T, Tsuji S et al (2007) Parietal dysgraphia: characterization of abnormal writing stroke sequences, character formation, and character recall. Behav Neurol 18:99–114
5. Alexander MP, Fischer RS, Friedman R (1992) Lesion localization in apractic agraphia. Arch Neurol 49:246–251
6. Heilman KM, Coenen A, Kluger B (2008) Progressive asymmetric apraxic agraphia. Cogn Behav Neurol 21:14–17
7. Passov V, Gavrilova RH, Strand E, Cerhan JH, Josephs KA (2011) Sporadic corticobasal syndrome with progranulin mutation presenting as progressive apraxic agraphia. Arch Neurol 68: 376–380
8. Kezuka M, Kawamura M, Yano Y, Shiroyama H (1995) A peculiar kind of agraphia due to degenerative processes predominant in the right hemisphere: comparison with apraxic agraphia. Shinkeishinrigaku 11:196–205
9. Croisile B, Brabant MJ, Carmoi T, Lepage Y, Aimard G, Trillet M (1996) Comparison between oral and written spelling in Alzheimer's disease. Brain Lang 54:361–387
10. Hughes JC, Graham N, Patterson K, Hodges JR (1997) Dysgraphia in mild dementia of Alzheimer's type. Neuropsychologia 35:533–545
11. Rapcsak SZ, Arthur SA, Bliklen DA, Rubens AB (1989) Lexical agraphia in Alzheimer's disease. Arch Neurol 46:65–68
12. Sakurai Y, Tsuchiya K, Oda T, Hori K, Tominaga I, Akiyama H et al (2006) Ubiquitin-positive frontotemporal lobar degeneration presenting with progressive Gogi (word-meaning) aphasia. A neuropsychological, radiological and pathological evaluation of a Japanese semantic dementia patient. J Neurol Sci 250:3–9
13. Ichikawa H, Takahashi N, Hieda S, Ohno H, Kawamura M (2008) Agraphia in bulbar-onset amyotrophic lateral sclerosis: not merely a consequence of dementia or aphasia. Behav Neurol 20:91–99
14. Sakurai Y, Hashida H, Uesugi H, Arima K, Murayama S, Bando M et al (1996) A clinical profile of corticobasal degeneration presenting as primary progressive aphasia. Eur Neurol 36:134–137

15. Platel H, Lambert J, Eustache F, Cadet B, Dary M, Viader F et al (1993) Characteristics and evolution of writing impairment in Alzheimer's disease. Neuropsychologia 31:1147–1158
16. Neils J, Roeltgen DP, Constantinidou F (1995) Decline in homophone spelling associated with loss of semantic influence on spelling in Alzheimer's disease. Brain Lang 49:27–49
17. Doody RS, Jankovic J (1992) The alien hand and related signs. J Neurol Neurosurg Psychiatry 55:806–810
18. Sakurai Y, Sakai K, Sakuta M, Iwata M (1994) Naming difficulties in alexia with agraphia for kanji after a left posterior inferior temporal lesion. J Neurol Neurosurg Psychiatry 57:609–613
19. Sakurai Y, Yagishita A, Goto Y, Ohtsu H, Mannen T (2006) Fusiform type alexia: pure alexia for words in contrast to posterior occipital type pure alexia for letters. J Neurol Sci 247:81–92
20. Sakurai Y, Matsumura K, Iwatsubo T, Momose T (1997) Frontal pure agraphia for kanji or kana: dissociation between morphology and phonology. Neurology 49:946–952
21. Dubois B, Slachevsky A, Litvan I, Pillon B (2000) The FAB: a frontal assessment battery at bedside. Neurology 55:1621–1626
22. Shaw LM, Vanderstichele H, Knapik-Czajka M, Clark CM, Aisen PS, Petersen RC et al (2009) Cerebrospinal fluid biomarker signature in Alzheimer's disease neuroimaging initiative subjects. Ann Neurol 65:403–413
23. Schoonenboom NS, Reesink FE, Verwey NA, Kester MI, Teunissen CE, van de Ven PM et al (2012) Cerebrospinal fluid markers for differential dementia diagnosis in a large memory clinic cohort. Neurology 78:47–54
24. Friston KJ, Holmes AP, Worsley KJ, Poline J-P, Frith CD, Frackowiak RSJ (1995) Statistical parametric maps in functional imaging: a general linear approach. Hum Brain Mapp 2:189–210
25. Matsuda H, Mizumura S, Soma T, Takemura N (2004) Conversion of brain SPECT images between different collimators and reconstruction processes for analysis using statistical parametric mapping. Nucl Med Commun 25:67–74
26. Crary MA, Heilman KM (1988) Letter imagery deficits in a case of pure apraxic agraphia. Brain Lang 34:147–156
27. Levine DN, Mani RB, Calvanio R (1988) Pure agraphia and Gerstmann's syndrome as a visuospatial–language dissociation: an experimental case study. Brain Lang 35:172–196
28. Boeve BF, Lang AE, Litvan I (2003) Corticobasal degeneration and its relationship to progressive supranuclear palsy and frontotemporal dementia. Ann Neurol 54(Suppl 5):S15–S19
29. Ishii K (2002) Clinical application of positron emission tomography for diagnosis of dementia. Ann Nucl Med 16:515–525
30. Hassan A, Whitwell JL, Josephs KA (2011) The corticobasal syndrome-Alzheimer's disease conundrum. Expert Rev Neurother 11:1569–1578
31. McKhann GM, Knopman DS, Chertkow H, Hyman BT, Jack CR Jr, Kawas CH et al (2011) The diagnosis of dementia due to Alzheimer's disease: recommendations from the National Institute on Aging-Alzheimer's Association workgroups on diagnostic guidelines for Alzheimer's disease. Alzheimers Dement 7: 263–269
32. Blennow K, Hampel H (2003) CSF markers for incipient Alzheimer's disease. Lancet Neurol 2:605–613
33. Moghekar A, Goh J, Li M, Albert M, O'Brien RJ (2012) Cerebrospinal fluid Abeta and tau level fluctuation in an older clinical cohort. Arch Neurol 69:246–250
34. Grimmer T, Riemenschneider M, Forstl H, Henriksen G, Klunk WE, Mathis CA et al (2009) Beta amyloid in Alzheimer's disease: increased deposition in brain is reflected in reduced concentration in cerebrospinal fluid. Biol Psychiatry 65:927–934
35. Shelley BP, Hodges JR, Kipps CM, Xuereb JH, Bak TH (2009) Is the pathology of corticobasal syndrome predictable in life? Mov Disord 24:1593–1599
36. Josephs KA, Whitwell JL, Boeve BF, Knopman DS, Petersen RC, Hu WT et al (2010) Anatomical differences between CBS-corticobasal degeneration and CBS-Alzheimer's disease. Mov Disord 25:1246–1252
37. Kim J, Basak JM, Holtzman DM (2009) The role of apolipoprotein E in Alzheimer's disease. Neuron 63:287–303
38. Christensen DZ, Schneider-Axmann T, Lucassen PJ, Bayer TA, Wirths O (2010) Accumulation of intraneuronal Abeta correlates with ApoE4 genotype. Acta Neuropathol 119:555–566
39. Cordato NJ, Halliday GM, McCann H, Davies L, Williamson P, Fulham M et al (2001) Corticobasal syndrome with tau pathology. Mov Disord 16:656–667
40. Boeve BF, Maraganore DM, Parisi JE, Ahlskog JE, Graff-Radford N, Caselli RJ et al (1999) Pathologic heterogeneity in clinically diagnosed corticobasal degeneration. Neurology 53:795–800
41. Williams DR, Holton JL, Strand K, Revesz T, Lees AJ (2007) Pure akinesia with gait freezing: a third clinical phenotype of progressive supranuclear palsy. Mov Disord 22:2235–2241
42. Yoshida T, Yamadori A, Mori E (1989) A case of micrographia with the right hand due to left putaminal infarction. Rinsho Shinkeigaku 29:1149–1151
43. Sakurai Y, Yoshida Y, Sato K, Sugimoto I, Mannen T (2011) Isolated thalamic agraphia with impaired grapheme formation and micrographia. J Neurol 258:1528–1537
44. Scarmeas N, Hadjigeorgiou GM, Papadimitriou A, Dubois B, Sarazin M, Brandt J et al (2004) Motor signs during the course of Alzheimer disease. Neurology 63:975–982
45. Heilman KM, Rothi LJ (2011) Apraxia. In: Heilman KM, Valenstein E (eds) Clinical neuropsychology, 5th edn. Oxford University Press, New York, pp 214–237
46. Sugishita M (1986) The Western Aphasia Battery, Japanese edn. Igaku-Shoin, Tokyo

Journal of Nuclear Medicine, published on April 14, 2014 as doi:10.2967/jnumed.113.133793

Quantitative Analysis of Amyloid Deposition in Alzheimer Disease Using PET and the Radiotracer ^{11}C-AZD2184

Hiroshi Ito[1], Hitoshi Shimada[1], Hitoshi Shinotoh[1], Harumasa Takano[1], Takeshi Sasaki[1], Tsuyoshi Nogami[1], Masayuki Suzuki[1], Tomohisa Nagashima[1], Keisuke Takahata[1], Chie Seki[1], Fumitoshi Kodaka[1], Yoko Eguchi[1], Hironobu Fujiwara[1], Yasuyuki Kimura[1], Shigeki Hirano[1], Yoko Ikoma[1], Makoto Higuchi[1], Kazunori Kawamura[1], Toshimitsu Fukumura[1], Éva Lindström Böö[2], Lars Farde[2], and Tetsuya Suhara[1]

[1]*Molecular Imaging Center, National Institute of Radiological Sciences, Chiba, Japan; and* [2]*AstraZeneca Translational Sciences Center, Department of Clinical Neuroscience, Karolinska Institutet, Stockholm, Sweden*

Characteristic neuropathologic changes in Alzheimer disease (AD) are amyloid-β deposits and neurofibrillary tangles. Recently, a new radioligand for amyloid senile plaques, ^{11}C-labeled 5-(6-{[tert-butyl(dimethyl)silyl]oxy}-1,3-benzothiazol-2-yl)pyridin-2-amine (^{11}C-AZD2184), was developed, and it was reported to show rapid brain uptake followed by rapid washout. In this study, ^{11}C-AZD2184 binding in control subjects and AD patients was examined in more detail by compartment model analysis using a metabolite-corrected arterial input function. The accuracy of simplified quantitative methods using a reference brain region was also evaluated. **Methods:** After intravenous bolus injection of ^{11}C-AZD2184, a dynamic PET scan was obtained for 90 min in 6 control subjects and 8 AD patients. To obtain the arterial input function, arterial blood sampling and high-performance liquid chromatography analysis were performed. **Results:** Time–activity curves in all brain regions could be described using the standard 2-tissue-compartment model. The total distribution volume ratios to reference region (*DVR*) in cerebral cortical regions were significantly higher in AD patients than in control subjects. Although there was no conspicuous accumulation of radioactivity in white matter as compared with other amyloid radioligands, *DVR* values in the centrum semiovale were more than 1 for both control subjects and AD patients, suggesting binding to myelin. The standardized uptake value ratio calculated from integrated time–activity curves in brain regions and the reference region was statistically in good agreement with *DVR*. **Conclusion:** Although the white matter binding of ^{11}C-AZD2184 may have some effect on cortical measurement, it can be concluded that the kinetic behavior of ^{11}C-AZD2184 is suitable for quantitative analysis. The standardized uptake value ratio can be used as a validated measure of ^{11}C-AZD2184 binding in clinical examinations without arterial input function.

Key Words: amyloid; Alzheimer; PET; AZD2184

J Nucl Med 2014; 55:1–7
DOI: 10.2967/jnumed.113.133793

Alzheimer disease (AD) is the most common neurodegenerative disorder. Characteristic neuropathologic changes in AD are amyloid-β deposits and neurofibrillary tangles (*1*). The amyloid cascade hypothesis states that the deposition of amyloid-β drives the remaining Alzheimer pathology, for example, formation of neurofibrillary tangles, cell loss, and vascular damage (*2*). From this perspective, in vivo imaging of amyloid-β deposits may contribute to early diagnosis of AD and serve as a marker for evaluation of disease-modifying drugs. To measure amyloid-β deposits by PET, several radiotracers, for example, ^{11}C-Pittsburgh compound B (^{11}C-PIB) (*3,4*) and (*E*)-4-(2-(6-(2-(2-(2-^{18}F-fluoroethoxy)ethoxy)ethoxy)pyridin-3-yl)vinyl)-*N*-methyl benzenamine (*5*), have been developed and used for examination of the pathophysiology of AD.

^{11}C-labeled 5-(6-{[tert-butyl(dimethyl)silyl]oxy}-1,3-benzothiazol-2-yl)pyridin-2-amine (^{11}C-AZD2184) is a more recently developed radiotracer for amyloid-β deposits. ^{11}C-AZD2184 has been characterized in preclinical studies and has high affinity in vitro for amyloid fibrils (dissociation constant, 8.4 ± 1.0 nM) (*6*). After intravenous injection of ^{11}C-AZD2184 in an initial human study, there was rapid uptake of radioactivity in the brain, followed by rapid washout in control subjects and in AD patients (*7*). The ratios of uptake in cortical regions to a reference brain region devoid of amyloid-β deposition were close to unity in control subjects and high in AD patients. In addition, there was no conspicuous accumulation of radioactivity in white matter.

The initial results indicate that ^{11}C-AZD2184 has potential as a sensitive imaging biomarker for research on the pathophysiology and treatment of AD. The aim of the present study was to examine ^{11}C-AZD2184 binding in greater detail by compartment model analysis using a metabolite-corrected arterial input function. The accuracy of simplified quantitative methods using a reference brain region was also evaluated.

MATERIALS AND METHODS

Subjects

Six control subjects (mean age ± SD, 65 ± 10 y) and 8 AD patients (72 ± 12 y) were recruited (Table 1). All AD patients were diagnosed according to the criteria of the National Institute of Neurologic and Communicative Diseases and Stroke/Alzheimer Disease and Related Disorders Association (*8*). All subjects were characterized according to the Clinical Dementia Rating scale (*9*). The control subjects were rated as 0 by the Clinical Dementia Rating scale, whereas the AD subjects were rated as 0.5, 1, or 2. In addition, the Mini-Mental State Examination was performed in [Table 1]

Received Oct. 10, 2013; revision accepted Jan. 27, 2013.
For correspondence or reprints contact: Hiroshi Ito, Biophysics Program, Molecular Imaging Center, National Institute of Radiological Sciences, 4-9-1 Anagawa, Inage-ku, Chiba 263-8555, Japan.
E-mail: hito@nirs.go.jp
Published online ••••••••••••.

TABLE 1
Profiles of Subjects

Subject group	Subject no.	Age (y)	Sex	Mini-Mental State Examination score	Clinical Dementia Rating scale
Control	NC1	61	F	28	0
	NC2	51	M	29	0
	NC3	60	M	30	0
	NC4	74	M	29	0
	NC5	71	M	28	0
	NC6	75	F	29	0
AD	AD1	76	F	15	1
	AD2	55	F	24	1
	AD3	63	M	13	1
	AD4	75	M	20	0.5
	AD5	84	F	13	1
	AD6	82	F	23	0.5
	AD7	82	F	19	1
	AD8	58	M	13	1

all subjects (*10*). No subject had any observable organic brain lesion according to MR imaging. Control subjects had no cognitive impairment and were free from medications for the central nervous system. The study was approved by the Institutional Review Board of the National Institute of Radiologic Sciences, Chiba, Japan. Written informed consent was obtained from all subjects or from their spouses or other close family members.

Radioligand

^{11}C-AZD2184 was produced according to the literature (*11*). In brief, ^{11}C-AZD2184 was radiosynthesized by reaction of the precursor 5-(6-(tert-butyldimethyl-silyloxy)benzo[d]thiazol-2-yl)pyridin-2-amine with ^{11}C-CH_3I in the presence of potassium hydroxide and subsequent deprotection by water (*7*).

PET Experimental Procedure

All PET measurements were performed with a SET-3000GCT/X scanner (Shimadzu Corp.) (*12*), which provides 99 sections with an axial field of view of 26 cm. The intrinsic spatial resolution is 3.4 mm in-plane and 5.0 mm in full width at half maximum axially. Images were reconstructed by the filtered backprojection algorithm. With a gaussian filter (cutoff frequency, 0.3 cycle/pixel), the reconstructed in-plane resolution was 7.5 mm in full width at half maximum. Data were acquired in 3-dimensional mode. Scatter correction was done by a hybrid scatter-correction method based on acquisition with dual-energy window setting (*13*). A 4-min transmission scan using a ^{137}Cs line source was obtained to correct for attenuation.

After intravenous bolus injection of ^{11}C-AZD2184 over 1 min, a dynamic PET scan was obtained for 90 min. The frame sequence consisted of six 10-s, three 20-s, six 1-min, four 3-min, and fourteen 5-min frames. The radioactivity injected was 380 ± 12 and 380 ± 13 MBq, and the specific radioactivity was 131 ± 38 and 119 ± 28 GBq/μmol at the time of injection for control subjects and AD patients, respectively.

To obtain the arterial input function, 32 samples of arterial blood were taken after injection. The fraction of radioactivity representing unchanged ^{11}C-AZD2184 in plasma was determined by high-performance

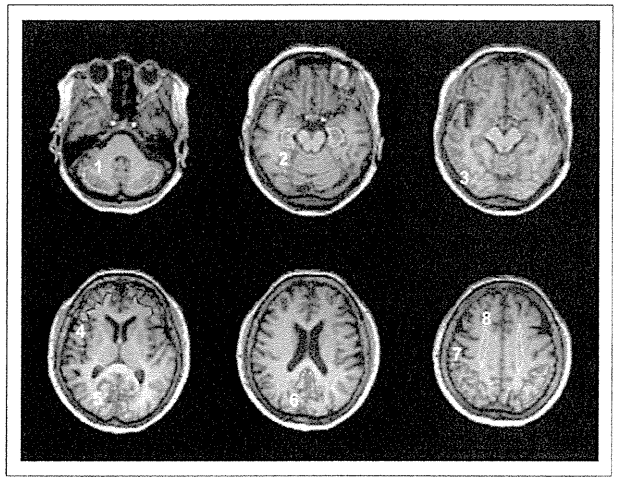

FIGURE 1. ROIs drawn on coregistered MR images. ROIs are defined for cerebellar cortex (1), parahippocampal gyrus including hippocampus (2), lateral side of temporal cortex (3), base side of frontal cortex (4), cuneus of occipital cortex (5), posterior region of cingulate gyrus (6), parietal cortex (7), and centrum semiovale (8).

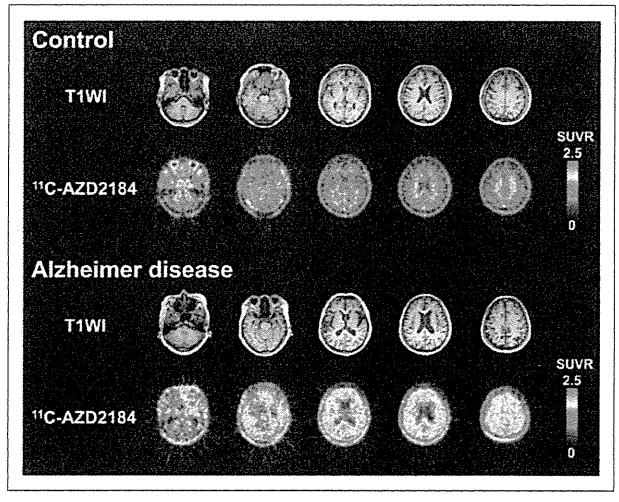

FIGURE 2. Representative *SUVR* images of ^{11}C-AZD2184 binding in control subject and AD patient. Integration interval was 40–60 min. Corresponding MR images (T1-weighted [T1WI]) are shown. Scale maximum and minimum values are 2.5 and 0 of *SUVR*. All images are transaxial sections, and anterior is at top of image and subjects' right is at left.

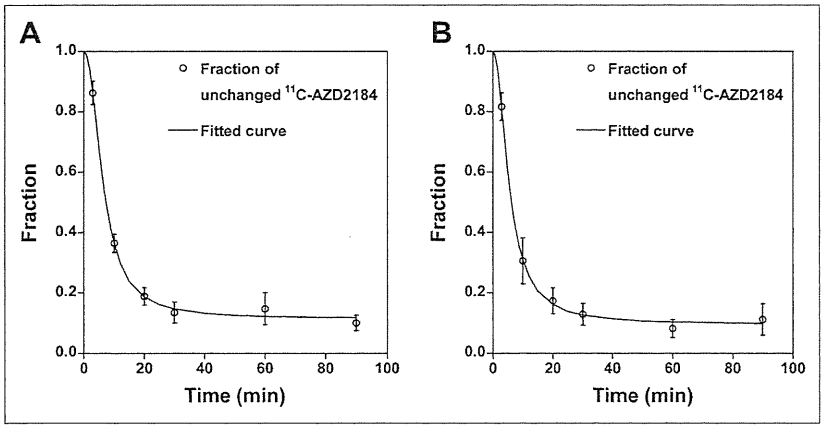

FIGURE 3. Time courses of fraction of radioactivity representing unchanged ^{11}C-AZD2184 in plasma for control subjects (A) and AD patients (B). Values are mean ± SD. Fitted curves were obtained using Hill equation.

liquid chromatography from 6 blood samples for each subject. Acetonitrile was added to each plasma sample, and the samples were then centrifuged. The obtained supernatant was subjected to radio–high-performance liquid chromatography analysis (column, μBondapak [10 μm, 7.8 × 300 nm]; Waters) (mobile phase, 90% acetonitrile [A]/1 mol/L ammonium formate [B]; gradient, 0–10 min [A/B], 22/78–47/53, 10–11 min [A/B], 47/53–80/20, and 11–12 min [A/B], 80/20–22/78; isocratic, 12–15 min end; flow rate, 6.0 mL/min). Plasma protein binding was not determined in the present study. The time curves for the fraction of unchanged ^{11}C-AZD2184 in plasma were fitted by the Hill equation and used for kinetic analysis.

MR Imaging Procedure

All MR imaging examinations were performed with a 3-T MR scanner (GE Healthcare). Three-dimensional volumetric acquisition of a T1-weighted 3-dimensional fast spoiled gradient-recalled acquisition in the steady-state sequence produced a gapless series of thin transverse sections (echo time, 2.848 ms; repetition time, 6.992 ms; prep time, 900 ms; flip angle, 8°; field of view, 260 mm; acquisition matrix, 256 × 256; slice thickness, 1 mm; scan time, 367 s). Proton density–weighted and T2-weighted images were obtained by a 2-dimensional double-echo fast spin echo sequence with interleaved and gapless acquisition (echo time for proton density–weighted images, 10.58 ms; effective echo time for T2-weighted images, 95.22 ms; repetition time, 3,000.00 ms; field of view, 240 mm; acquisition matrix, 256 × 256; slice thickness, 3 mm [no gap, interleave]; echo train length, 16; scan time, 309 s). T1-weighted images were used for analysis of PET images. Proton density–weighted and T2-weighted images were used to confirm whether subjects had any observable organic brain lesion.

Regions of Interest (ROIs)

All MR images were coregistered to the individual PET images using the software package PMOD (version 3.0; PMOD Technologies Ltd.). ROIs were drawn on coregistered MR images (T1-weighted images) and transferred to the PET images. ROIs were defined for the cerebellar cortex, parahippocampal gyrus including the hippocampus, posterior region of the cingulate gyrus, base side of the frontal cortex, lateral side of the temporal cortex, parietal cortex, cuneus of the occipital cortex, and centrum semiovale (Fig. 1). Each ROI was drawn on 3 adjacent sections, and data were pooled to obtain the average radioactivity concentration for the whole volume of interest. To obtain regional time–activity curves, regional radioactivity was calculated for each frame, corrected for decay, and plotted versus time. [Fig. 1]

Kinetic Model for Interpretation of ^{11}C-AZD2184 Binding

To interpret the kinetic behavior of ^{11}C-AZD2184, the standard 2-tissue-compartment model with 4 first-order rate constants was used (*14*). The rate constants K_1 and k_2 describe the influx and efflux rates for radiotracer diffusion through the blood–brain barrier, respectively. The rate constants k_3 and k_4 describe the radiotracer transfer between the compartments for nondisplaceable radiotracer and specific binding. The distribution volume with only nondisplaceable binding in a brain region (V_{ND}), the total distribution volume (V_T), and the binding potential relative to the concentration of nondisplaceable radiotracer in brain (BP_{ND}) are expressed as follows (*15*):

$$V_{ND} = \frac{K_1}{k_2} \qquad \text{Eq. 1}$$

$$V_T = \frac{K_1}{k_2}\left(1 + \frac{k_3}{k_4}\right) \qquad \text{Eq. 2}$$

$$BP_{ND} = \frac{k_3}{k_4} \qquad \text{Eq. 3}$$

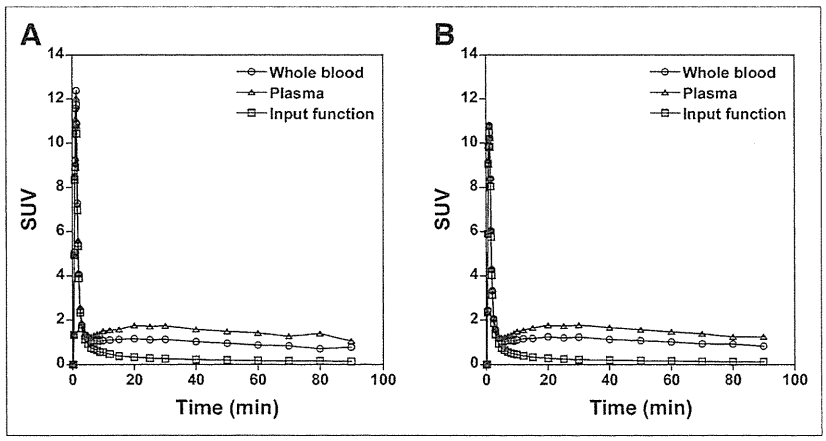

FIGURE 4. Time courses of average radioactivity concentration in arterial whole blood and plasma for control subjects (A) and AD patients (B). Time courses of average radioactivity concentration of unchanged ^{11}C-AZD2184 in plasma (i.e., arterial input function) are also shown.

Kinetic Analysis of ^{11}C-AZD2184 Binding

To estimate the rate constants (K_1, k_2, k_3, and k_4), nonlinear curve fitting was performed in a least-squares sense to the regional time–activity curves (*16*). In this analysis, the blood volume, which depends on the first-pass extraction fraction of the tracer, was assumed to be 0.04 mL/mL to diminish the influence of tracer remaining in the blood using the radioactivity of whole blood (*17*). The radioactivity of unchanged ^{11}C-AZD2184

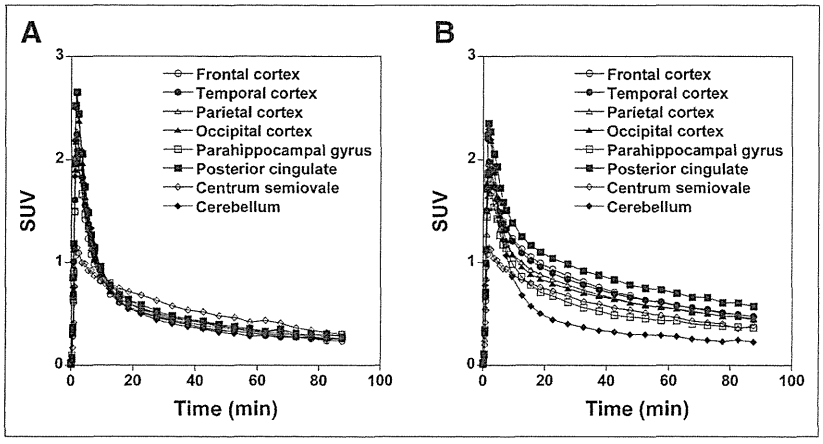

FIGURE 5. Average time–activity curves for brain regions in control subjects (A) and AD patients (B).

in plasma was used as the arterial input function. For this analysis, PMOD was used. V_T was calculated from the rate constants as an indicator of amyloid-β deposits (Eq. 2).

Quantitative Approach Using Reference Region

The cerebellum has been suggested as a reference brain region because no fibrillar amyloid plaques have been demonstrated in this region postmortem (*18,19*). A quantitative approach, taking advantage of the cerebellum as a reference region, can be used to calculate the total distribution volume ratio (*DVR*) as follows:

$$DVR = V_{T(brain)}/V_{T(cerebellum)}, \quad \text{Eq. 4}$$

where $V_{T(brain)}$ and $V_{T(cerebellum)}$ are total distribution volume in brain regions and the cerebellum, respectively. The BP_{ND} is equal to $DVR - 1$ if the cerebellum is the ideal reference brain region.

In addition, the standardized uptake value (*SUV*) was calculated from the time-integrated regional radioactivity concentration normalized with injected dose per body weight. The integration intervals were 20–40, 40–60, and 60–90 min. The integration interval of 20–40 min includes the peak equilibrium condition (*20*), and the integration intervals of 40–60 and 60–90 min correspond to the late part of the time–activity curve. In a simplified approach and because the cerebellum can be used as a reference brain region, the *SUV* ratio (*SUVR*) indicating amyloid-β deposits was calculated using the following expression:

$$SUVR = SUV_{brain}/SUV_{cerebellum}, \quad \text{Eq. 5}$$

where SUV_{brain} and $SUV_{cerebellum}$ represent the *SUV* in brain regions and the cerebellum, respectively.

RESULTS

In this study, no adverse event was observed after intravenous injection of ^{11}C-AZD2184. Representative *SUVR* images showing the distribution of brain radioactivity after intravenous injection of ^{11}C-AZD2184 are shown for a control subject and an AD patient [Fig. 2] in Figure 2. There was no conspicuous accumulation of radioactivity in white matter, the same as in a previous report (*7*). In AD patients, radioactivity in the cerebral cortices was higher than in the control subjects. By visual assessment of the *SUVR* images, all control subjects appeared negative with regard to specific binding of ^{11}C-AZD2184, whereas all AD patients appeared positive.

The time courses for the average fraction of radioactivity representing unchanged ^{11}C-AZD2184 in plasma for control subjects and AD patients are shown in Figure 3. [Fig. 3] Sixty minutes after injection of ^{11}C-AZD2184, the fraction of radioactivity representing unchanged ^{11}C-AZD2184 in plasma was 0.11–0.12. The time courses of the average radioactivity concentration in whole blood and plasma and the time course of the radioactivity concentration of unchanged ^{11}C-AZD2184 in plasma (i.e., arterial input function) are shown in Figure 4. [Fig. 4]

The regional time–activity curves for control subjects and AD patients are shown in Figure 5. At 18.5, 37.5, 57.5, and 87.5 min after injection of [Fig. 5] ^{11}C-AZD2184, the ratios of regional radioactivity of posterior cingulate to cerebellum were 1.14 ± 0.03, 1.21 ± 0.09, 1.27 ± 0.17, and 1.08 ± 0.27 for control subjects and 2.19 ± 0.22, 2.60 ± 0.57, 2.55 ± 0.49, and 2.52 ± 0.64 for AD patients. In control subjects, radioactivity concentrations in cerebral cortical regions were similar to those for the cerebellum at the end of data acquisition, the same as in a previous report (*7*). In AD patients, radioactivity concentrations in cerebral cortical regions were higher than in the cerebellum.

Typical time–activity curves in brain regions of an AD patient and the corresponding fitted curves obtained by kinetic analyses are shown in Figure 6. The time–activity curves in all brain [Fig. 6] regions could be described by the standard 2-tissue-compartment model.

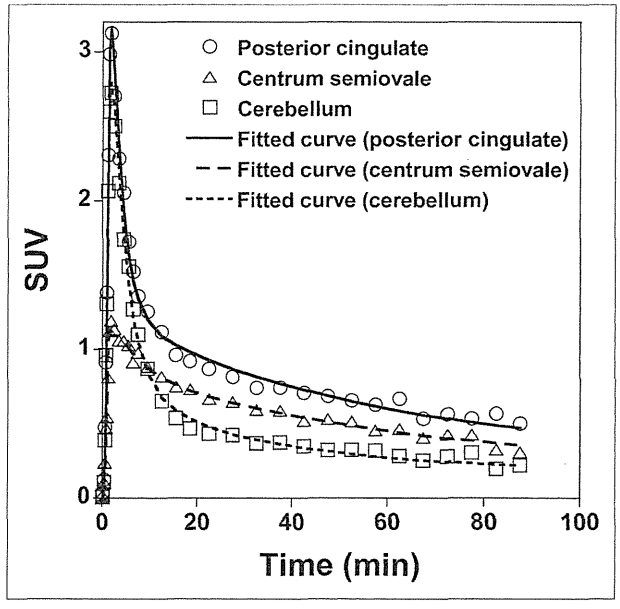

FIGURE 6. Typical time–activity curves in brain regions of AD patient and fitted curves obtained using standard 2-tissue-compartment model.

jnm133793-pm ■ 4/7/14

TABLE 2
Kinetic Parameters Obtained by 2-Tissue-Compartment Model Analysis of ^{11}C-AZD2184 Binding in Control Subjects

Brain region	K_1 (mL/mL/min)	k_2 (min^{-1})	k_3 (min^{-1})	k_4 (min^{-1})	V_T (mL/mL)	*DVR*
Frontal cortex	0.23 ± 0.07	0.42 ± 0.09	0.05 ± 0.02	0.05 ± 0.02	1.14 ± 0.19	0.99 ± 0.07
Temporal cortex	0.25 ± 0.07	0.42 ± 0.09	0.06 ± 0.02	0.05 ± 0.02	1.22 ± 0.17	1.07 ± 0.06
Parietal cortex	0.25 ± 0.06	0.43 ± 0.08	0.05 ± 0.02	0.05 ± 0.02	1.18 ± 0.17	1.03 ± 0.09
Occipital cortex	0.32 ± 0.07	0.53 ± 0.12	0.05 ± 0.02	0.04 ± 0.01	1.28 ± 0.17	1.12 ± 0.09
Hippocampus	0.22 ± 0.05	0.41 ± 0.12	0.08 ± 0.04	0.06 ± 0.02	1.27 ± 0.19	1.11 ± 0.07
Posterior cingulate	0.32 ± 0.09	0.52 ± 0.11	0.06 ± 0.03	0.06 ± 0.03	1.33 ± 0.23	1.16 ± 0.11
Centrum semiovale	0.09 ± 0.03	0.17 ± 0.08	0.09 ± 0.04	0.05 ± 0.01	1.50 ± 0.31	1.30 ± 0.12
Cerebellum	0.28 ± 0.06	0.38 ± 0.05	0.03 ± 0.02	0.05 ± 0.02	1.15 ± 0.22	—

Values are mean ± SD.

The rate constants and related kinetic parameters for ^{11}C-AZD2184 binding in control subjects and AD patients are given [Table 2] in Tables 2 and 3, respectively. In control subjects, the V_T in [Table 3] cerebral cortical regions was similar to that in the cerebellum. In AD patients, V_T values were consistently higher in cerebral cortical regions than in the cerebellum. The V_T and the *DVR* in cerebral cortical regions were significantly higher in AD patients than in control subjects (unpaired *t* test, $P < 0.01$). The *DVR* in the centrum semiovale was more than 1 in average for both control subjects and AD patients. No significant differences in V_T and *DVR* were observed for the centrum semiovale between control subjects and AD patients.

The *SUVR* and *DVR* in control subjects and AD patients are [Table 4] shown in Table 4. The *SUVR* for each integration interval was at the same level and in agreement with the corresponding *DVR* value. *SUVR* and *DVR* in cerebral cortical regions were significantly higher in AD patients than in control subjects. The relation- [Fig. 7] ship between *DVR* and *SUVR* is shown in Figure 7. Significant correlations were observed between *DVR* and *SUVR* for each integration interval.

DISCUSSION

In the present examination of ^{11}C-AZD2184 binding to amyloid-β deposits, there was high binding in the cerebral cortical regions of AD patients in comparison with control subjects, the same as in a previous report (*7*). The *DVR* values of ^{11}C-AZD2184 in cerebral cortical regions for both control subjects and AD patients were almost the same level as those of ^{11}C-PIB reported previously (*18*). Although previously developed radioligands, such as ^{11}C-PIB, show high nonspecific binding in white matter, the white matter binding was not conspicuous for ^{11}C-AZD2184. The *SUV*s in the white matter were less than 0.5 after 60 min of injection of ^{11}C-AZD2184 in both control subjects and AD patients, and those of ^{11}C-PIB were reported to be more than 1 (*4*). The regional time–activity curves could be described by the standard 2-tissue-compartment model. The dissociation rate constant k_4 was 0.04–0.05 min^{-1}, not zero, indicating reversibility of binding. Thus, it was evident that the kinetic behavior of ^{11}C-AZD2184 is similar to that of established neuroreceptor ligands such as ^{11}C-raclopride (*20*) and that this radioligand is likely suitable for quantitative analyses using various established approaches.

The white matter binding of ^{11}C-AZD2184 appears lower than that reported for other amyloid radioligands such as ^{11}C-PIB (*4*), the same as in the previous autoradiographic study with postmortem brain (*6*). In control subjects, there was no obvious difference between binding in gray and white matter. However, kinetic analysis revealed the *DVR* to be more than 1 (~1.3–1.5) in the centrum semiovale, a region that almost entirely consists of white matter, for both control subjects and AD patients. The nature of the binding of amyloid ligand to white matter is not fully understood. It has been reported that ^{11}C-PIB may bind to myelin, which is organized in a β-sheet structure in the same way as amyloid-β deposits (*21–23*). The proposed binding has low affinity and is likely not saturable because of the large amount of myelin in the brain. In other words, a high concentration of unlabeled ligand would be required to saturate the binding of amyloid

TABLE 3
Kinetic Parameters Obtained by 2-Tissue-Compartment Model Analysis of ^{11}C-AZD2184 Binding in AD Patients

Brain region	K_1 (mL/mL/min)	k_2 (min^{-1})	k_3 (min^{-1})	k_4 (min^{-1})	V_T (mL/mL)	*DVR*
Frontal cortex	0.21 ± 0.04	0.27 ± 0.08	0.09 ± 0.02	0.04 ± 0.01	2.49 ± 0.48	1.96 ± 0.25
Temporal cortex	0.22 ± 0.05	0.27 ± 0.09	0.08 ± 0.01	0.04 ± 0.01	2.48 ± 0.43	1.97 ± 0.26
Parietal cortex	0.18 ± 0.05	0.25 ± 0.10	0.07 ± 0.02	0.04 ± 0.01	2.30 ± 0.47	1.84 ± 0.37
Occipital cortex	0.28 ± 0.05	0.39 ± 0.10	0.07 ± 0.02	0.03 ± 0.01	2.35 ± 0.54	1.86 ± 0.33
Hippocampus	0.21 ± 0.03	0.32 ± 0.08	0.07 ± 0.02	0.04 ± 0.02	1.81 ± 0.33	1.43 ± 0.15
Posterior cingulate	0.26 ± 0.06	0.30 ± 0.10	0.08 ± 0.02	0.04 ± 0.01	3.04 ± 0.77	2.39 ± 0.42
Centrum semiovale	0.10 ± 0.02	0.14 ± 0.03	0.08 ± 0.05	0.05 ± 0.03	1.94 ± 0.54	1.51 ± 0.22
Cerebellum	0.28 ± 0.05	0.37 ± 0.08	0.03 ± 0.02	0.06 ± 0.05	1.27 ± 0.20	—

Values are mean ± SD.

TABLE 4
*SUVR*s of ^{11}C-AZD2184 in Control Subjects and AD Patients

	Control				AD			
	SUVR				*SUVR*			
Brain region	20–40 min*	40–60 min*	60–90 min*	*DVR*	20–40 min*	40–60 min*	60–90 min*	*DVR*
Frontal cortex	1.04 ± 0.04	1.07 ± 0.09	0.99 ± 0.10	0.99 ± 0.07	2.16 ± 0.28†	2.17 ± 0.27†	2.13 ± 0.28†	1.96 ± 0.25†
Temporal cortex	1.10 ± 0.04	1.14 ± 0.04	1.08 ± 0.07	1.07 ± 0.06	2.09 ± 0.23†	2.14 ± 0.25†	2.15 ± 0.30†	1.97 ± 0.26†
Parietal cortex	1.06 ± 0.07	1.08 ± 0.10	1.03 ± 0.09	1.03 ± 0.09	1.93 ± 0.30†	1.98 ± 0.38†	2.01 ± 0.44†	1.84 ± 0.37†
Occipital cortex	1.13 ± 0.06	1.21 ± 0.08	1.11 ± 0.10	1.12 ± 0.09	1.87 ± 0.38†	1.97 ± 0.33†	2.01 ± 0.38†	1.86 ± 0.33†
Hippocampus	1.15 ± 0.07	1.18 ± 0.05	1.15 ± 0.07	1.11 ± 0.07	1.52 ± 0.11†	1.52 ± 0.15†	1.58 ± 0.16†	1.43 ± 0.15†
Posterior cingulate	1.19 ± 0.08	1.24 ± 0.13	1.17 ± 0.12	1.16 ± 0.11	2.46 ± 0.44†	2.54 ± 0.43†	2.56 ± 0.42†	2.39 ± 0.42†
Centrum semiovale	1.41 ± 0.08	1.49 ± 0.14	1.36 ± 0.17	1.30 ± 0.12	1.68 ± 0.19	1.72 ± 0.21	1.64 ± 0.22	1.51 ± 0.22

*Integration interval.
†Significant differences from normal control subjects (unpaired *t* test, $P < 0.01$).
Values are mean ± SD.

radioligands to cerebral white matter (*24*). Moreover, it has been estimated that ROIs defined for the cerebral cortex contain about 60% of gray matter and 30% of white matter (*25*). This tissue heterogeneity may affect ^{11}C-AZD2184 binding in the cerebral cortices.

To examine simplified approaches for quantification of ^{11}C-AZD2184 binding, the *SUVR* was calculated using the cerebellum as a reference brain region, with integration intervals of 20–40, 40–60, and 60–90 min. The *SUVR* of each integration interval was at the same level and statistically in good agreement with the *DVR* values obtained by kinetic analysis, although systemic overestimations in *SUVR* were observed. This cross-validation indicates that ^{11}C-AZD2184 binding can be estimated using a short scanning time and no arterial blood sampling. The nonlinearity and bias of *SUVR* as compared with *DVR* are observed in most radiotracers (*26,27*). However, the fast relative equilibrium of ^{11}C-AZD2184 could be one of the main advantages over ^{11}C-PIB (*4*). In further study, systemic errors in *SUVR* of ^{11}C-AZD2184 should be investigated with simulation studies. Although all integration intervals can be used to calculate *SUVR*, integration intervals of 40–60 and 60–90 min might be more preferable because the early part of the time–activity curve is generally affected by changes in K_1 due to changes in cerebral blood flow (*20*). However, a lack of an early phase of PET data might hamper an adequate coregistration between PET and MR images, especially in control subjects because of a low binding in the white matter.

It has been reported that synaptic loss is associated with nondiffuse plaques, but not with diffuse plaques (*28*), and that the neuropathology in AD is characterized by cortical neuritic plaque containing dense-cored amyloid deposition (*29*). ^{11}C-BF227, a recently developed radiotracer for in vivo imaging of amyloid-β, has been considered to bind more preferentially to dense-cored amyloid deposition than ^{11}C-PIB (*19*). Further research is needed to demonstrate the binding characteristics of ^{11}C-AZD2184 in different types of amyloid plaque.

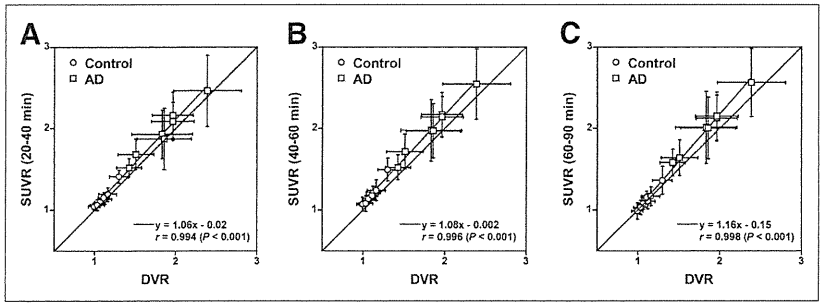

FIGURE 7. Relationship between *DVR* and *SUVR* for integration intervals of 20–40 min (A), 40–60 min (B), and 60–90 min (C). Respective data indicate mean and SD of each ROI.

CONCLUSION

The novel radioligand ^{11}C-AZD2184 provides high-contrast imaging of amyloid-β deposits in brain. The regional kinetics of ^{11}C-AZD2184 binding in control subjects and AD patients could be described by the standard 2-tissue-compartment model. The *SUVR* calculated from integrated time–activity curves in targeted and reference brain regions can be used as an index of ^{11}C-AZD2184 binding for clinical investigations without arterial input function.

DISCLOSURE

The costs of publication of this article were defrayed in part by the payment of page charges. Therefore, and solely to indicate this fact, this article is hereby marked "advertisement" in accordance with 18 USC section 1734. This study was supported in part by the "Japan Advanced Molecular Imaging Program (J-AMP)" of the Ministry of Education, Culture, Sports, Science and Technology (MEXT), Japanese Government, and a grant-in-aid for Comprehensive Research on Dementia (no. 11103404) from the Ministry of Health, Labor and Welfare. No other potential conflict of interest relevant to this article was reported.

ACKNOWLEDGMENTS

We thank Katsuyuki Tanimoto, Takahiro Shiraishi, Kazuko Suzuki, and Izumi Izumida for their assistance in the PET experiments. 5-(6-{[tert-butyl(dimethyl)silyl]oxy}-1,3-benzothiazol-2-yl)pyridin-2-amine (AZD2184) and its precursor 5-(6-(tert-butyldimethylsilyloxy)benzo[d]thiazol-2-yl)pyridin-2-amine were kindly provided by AstraZeneca R&D, Södertälje, Sweden.

REFERENCES

1. Braak H, Braak E. Neuropathological stageing of Alzheimer-related changes. *Acta Neuropathol.* 1991;82:239–259.
2. Hardy JA, Higgins GA. Alzheimer's disease: the amyloid cascade hypothesis. *Science.* 1992;256:184–185.
3. Mathis CA, Wang Y, Holt DP, Huang GF, Debnath ML, Klunk WE. Synthesis and evaluation of ^{11}C-labeled 6-substituted 2-arylbenzothiazoles as amyloid imaging agents. *J Med Chem.* 2003;46:2740–2754.
4. Klunk WE, Engler H, Nordberg A, et al. Imaging brain amyloid in Alzheimer's disease with Pittsburgh compound-B. *Ann Neurol.* 2004;55:306–319.
5. Choi SR, Golding G, Zhuang Z, et al. Preclinical properties of ^{18}F-AV-45: a PET agent for Aβ plaques in the brain. *J Nucl Med.* 2009;50:1887–1894.
6. Johnson AE, Jeppsson F, Sandell J, et al. AZD2184: a radioligand for sensitive detection of beta-amyloid deposits. *J Neurochem.* 2009;108:1177–1186.
7. Nyberg S, Jonhagen ME, Cselenyi Z, et al. Detection of amyloid in Alzheimer's disease with positron emission tomography using [^{11}C]AZD2184. *Eur J Nucl Med Mol Imaging.* 2009;36:1859–1863.
8. McKhann G, Drachman D, Folstein M, Katzman R, Price D, Stadlan EM. Clinical diagnosis of Alzheimer's disease: report of the NINCDS-ADRDA Work Group under the auspices of Department of Health and Human Services Task Force on Alzheimer's Disease. *Neurology.* 1984;34:939–944.
9. Morris JC. The Clinical Dementia Rating (CDR): current version and scoring rules. *Neurology.* 1993;43:2412–2414.
10. Folstein MF, Folstein SE, McHugh PR. "Mini-mental state": a practical method for grading the cognitive state of patients for the clinician. *J Psychiatr Res.* 1975;12:189–198.
11. Andersson JD, Varnas K, Cselenyi Z, et al. Radiosynthesis of the candidate beta-amyloid radioligand [^{11}C]AZD2184: positron emission tomography examination and metabolite analysis in cynomolgus monkeys. *Synapse.* 2010;64:733–741.
12. Matsumoto K, Kitamura K, Mizuta T, et al. Performance characteristics of a new 3-dimensional continuous-emission and spiral-transmission high-sensitivity and high-resolution PET camera evaluated with the NEMA NU 2-2001 standard. *J Nucl Med.* 2006;47:83–90.
13. Ishikawa A, Kitamura K, Mizuta T, et al. Implementation of on-the-fly scatter correction using dual-energy window method in continuous 3D whole body PET scanning. *IEEE Nucl Sci Symp Conf Rec.* 2005;5:2497–2500.
14. Mintun MA, Raichle ME, Kilbourn MR, Wooten GF, Welch MJ. A quantitative model for the in vivo assessment of drug binding sites with positron emission tomography. *Ann Neurol.* 1984;15:217–227.
15. Innis RB, Cunningham VJ, Delforge J, et al. Consensus nomenclature for in vivo imaging of reversibly binding radioligands. *J Cereb Blood Flow Metab.* 2007;27:1533–1539.
16. Marquardt D. An algorithm for least-squares estimation of nonlinear parameters. *J Soc Ind Appl Math.* 1963;11:431–441.
17. Ito H, Ota M, Ikoma Y, et al. Quantitative analysis of dopamine synthesis in human brain using positron emission tomography with L-[β-^{11}C]DOPA. *Nucl Med Commun.* 2006;27:723–731.
18. Price JC, Klunk WE, Lopresti BJ, et al. Kinetic modeling of amyloid binding in humans using PET imaging and Pittsburgh compound-B. *J Cereb Blood Flow Metab.* 2005;25:1528–1547.
19. Kudo Y, Okamura N, Furumoto S, et al. 2-(2-[2-dimethylaminothiazol-5-yl] ethenyl)-6- (2-[fluoro]ethoxy)benzoxazole: a novel PET agent for in vivo detection of dense amyloid plaques in Alzheimer's disease patients. *J Nucl Med.* 2007;48:553–561.
20. Ito H, Hietala J, Blomqvist G, Halldin C, Farde L. Comparison of the transient equilibrium and continuous infusion method for quantitative PET analysis of [^{11}C]raclopride binding. *J Cereb Blood Flow Metab.* 1998;18:941–950.
21. Klunk WE, Wang Y, Huang GF, et al. The binding of 2-(4'-methylaminophenyl) benzothiazole to postmortem brain homogenates is dominated by the amyloid component. *J Neurosci.* 2003;23:2086–2092.
22. Klunk WE, Lopresti BJ, Ikonomovic MD, et al. Binding of the positron emission tomography tracer Pittsburgh compound-B reflects the amount of amyloid-beta in Alzheimer's disease brain but not in transgenic mouse brain. *J Neurosci.* 2005;25:10598–10606.
23. Fodero-Tavoletti MT, Rowe CC, McLean CA, et al. Characterization of PiB binding to white matter in Alzheimer disease and other dementias. *J Nucl Med.* 2009;50:198–204.
24. Stankoff B, Freeman L, Aigrot MS, et al. Imaging central nervous system myelin by positron emission tomography in multiple sclerosis using [methyl-^{11}C]-2-(4'-methylaminophenyl)- 6-hydroxybenzothiazole. *Ann Neurol.* 2011;69:673–680.
25. Ito H, Takahashi H, Arakawa R, Takano H, Suhara T. Normal database of dopaminergic neurotransmission system in human brain measured by positron emission tomography. *Neuroimage.* 2008;39:555–565.
26. Ito H, Halldin C, Farde L. Localization of 5-HT_{1A} receptors in the living human brain using [carbonyl-^{11}C]WAY-100635: PET with anatomic standardization technique. *J Nucl Med.* 1999;40:102–109.
27. Zhou Y, Sojkova J, Resnick SM, Wong DF. Relative equilibrium plot improves graphical analysis and allows bias correction of standardized uptake value ratio in quantitative ^{11}C-PiB PET studies. *J Nucl Med.* 2012;53:622–628.
28. Masliah E, Terry RD, Mallory M, Alford M, Hansen LA. Diffuse plaques do not accentuate synapse loss in Alzheimer's disease. *Am J Pathol.* 1990;137:1293–1297.
29. Price JL. Diagnostic criteria for Alzheimer's disease. *Neurobiol Aging.* 1997;18:S67–S70.

Sato et al. EJNMMI Research 2013, 3:76
http://www.ejnmmires.com/content/3/1/76

EJNMMI Research
a SpringerOpen Journal

ORIGINAL RESEARCH Open Access

Noninvasive k_3 estimation method for slow dissociation PET ligands: application to [^{11}C] Pittsburgh compound B

Koichi Sato[1,2], Kiyoshi Fukushi[1], Hitoshi Shinotoh[1,3], Hitoshi Shimada[1,4], Shigeki Hirano[1,5], Noriko Tanaka[6], Tetsuya Suhara[1], Toshiaki Irie[1] and Hiroshi Ito[1*]

Abstract

Background: Recently, we reported an information density theory and an analysis of three-parameter plus shorter scan than conventional method (3P+) for the amyloid-binding ligand [^{11}C]Pittsburgh compound B (PIB) as an example of a non-highly reversible positron emission tomography (PET) ligand. This article describes an extension of 3P + analysis to noninvasive '3P++' analysis (3P + plus use of a reference tissue for input function).

Methods: In 3P++ analysis for [^{11}C]PIB, the cerebellum was used as a reference tissue (negligible specific binding). Fifteen healthy subjects (NC) and fifteen Alzheimer's disease (AD) patients participated. The k_3 (index of receptor density) values were estimated with 40-min PET data and three-parameter reference tissue model and were compared with that in 40-min 3P + analysis as well as standard 90-min four-parameter (4P) analysis with arterial input function. Simulation studies were performed to explain k_3 biases observed in 3P++ analysis.

Results: Good model fits of 40-min PET data were observed in both reference and target regions-of-interest (ROIs). High linear intra-subject (inter-15 ROI) correlations of k_3 between 3P++ (*Y*-axis) and 3P + (*X*-axis) analyses were shown in one NC ($r^2 = 0.972$ and slope = 0.845) and in one AD ($r^2 = 0.982$, slope = 0.655), whereas inter-subject k_3 correlations in a target region (left lateral temporal cortex) from 30 subjects (15 NC + 15 AD) were somewhat lower ($r^2 = 0.739$ and slope = 0.461). Similar results were shown between 3P++ and 4P analyses: $r^2 = 0.953$ for intra-subject k_3 in NC, $r^2 = 0.907$ for that in AD and $r^2 = 0.711$ for inter-30 subject k_3. Simulation studies showed that such lower inter-subject k_3 correlations and significant negative k_3 biases were not due to unstableness of 3P++ analysis but rather to inter-subject variation of both k_2 (index of brain-to-blood transport) and k_3 (not completely negligible) in the reference region.

Conclusions: In [^{11}C]PIB, the applicability of 3P++ analysis may be restricted to intra-subject comparison such as follow-up studies. The 3P++ method itself is thought to be robust and may be more applicable to other non-highly reversible PET ligands with ideal reference tissue.

Keywords: [^{11}C]Pittsburgh compound B; Alzheimer's disease; Kinetic modeling; PET quantification; Reference tissue; Slow dissociation ligand

* Correspondence: hito@nirs.go.jp
[1]Molecular Imaging Center, National Institute of Radiological Sciences, 4-9-1 Anagawa, Inage-ku, Chiba 260-8555, Japan
Full list of author information is available at the end of the article

Background

Various reversible-type radioligands have been developed for *in vivo* neuroreceptor study with positron emission tomography (PET). Both arterial blood sampling and long dynamic PET scan, up to 120 min, are required for standard nonlinear least-squares (NLS) analysis to estimate K_1 to k_4 in the two-tissue compartment four-parameter model (4P model): K_1 represents the blood-to-brain transport constant, k_2 represents the brain-to-blood transport constant, k_3 represents the first-order association rate constant for specific binding, and k_4 represents the dissociation rate constant for specific binding. The k_3 represents $B_{max} \cdot k_{on}$, where B_{max} is maximum receptor density and k_{on} is the *in vivo* association rate constant. Since k_3 represents available receptors for the PET ligand, it is the target parameter of major interest in most PET studies. However, quantification of k_3 in the 4P model is often difficult because of uncertainty of the k_4 estimate and high correlation between the k_3 and k_4 estimates. As surrogate parameters for B_{max}, binding potential and distribution volume have been widely used [1-4]. Several reference tissue methods have also been developed [5-10].

Irreversible (enzyme-substrate type) radiotracers [^{11}C] methylpiperidin-4-yl acetate and propionate have been developed for the measurement of cerebral acetylcholine esterase activity using PET [11,12]. In this case the two-tissue compartment three-parameter (K_1 to k_3) model (3P model) was used to estimate k_3, which is an index of acetylcholine esterase activity. In the 3P model, the precision of k_3 estimate is usually higher than in the 4P model, in spite of shorter PET scan time (40 to 60 min), since there is no need of k_4 estimation in the 3P model.

We have previously defined two mathematical functions, the information density function and information function, which are useful for model selection and optimization of scan time in PET [13]. Based on simulations using both functions, we proposed a new method (3P + method) for quantification of k_3 for moderately reversible ligands. '3P+' means three-parameter model plus short PET scan. In this method, the 3P model ($k_4 = 0$ model) was applied to the early-phase PET data (up to 30 to 40 min) from reversible ligands with moderate k_4 (moderately reversible ligands). Although the 3P + method was not always developed for a specific ligand, the amyloid-binding radiotracer [^{11}C]Pittsburgh compound B (PIB) was used as an example for the moderately reversible ligands (k_4 = 0.018/min). The 3P + method afforded a more stable k_3 estimate than the standard 90-min 4P analysis. However, there is still the drawback of the necessity for arterial blood sampling and radiometabolite analysis, which may restrict the widespread use of this method in daily clinical practice.

In this article, we propose a noninvasive 3P++ analysis using [^{11}C]PIB. 3P++ means 3P + analysis plus use of a reference tissue for input function. To validate the proposed method, the linear correlations of k_3 estimates were evaluated between 40-min 3P++ and 3P + analyses, as well as between 3P++ and 90-min 4P analyses in clinical PET studies. In addition, simulation studies were performed to explain k_3 biases observed in the 3P++ analysis.

Methods

Theory

Assumptions in 3P++ analysis

The following are assumptions used in 3P++ analysis:

- Assumption 1 (on the nature of radioligand used): We apply 3P++ analysis only to moderately reversible or nearly irreversible radioligands ($k_4 \leq 0.03$/min), but exclude highly reversible ligands. [^{11}C]PIB is an example of moderately reversible ligands ($k_4 = 0.018$/min).
- Assumption 2 (on the duration time of PET scan): We use early-phase PET data in the curve fitting. In [^{11}C]PIB, dynamic PET data during 0 to 40 min was described well with the 3P model, since the effect of the k_4 process on PET data was negligible within these early-phase kinetics [13].
- Assumption 3 (on the specific binding in the reference tissue, k_{3r}): Specific binding of radioligand is negligible in the reference tissue ($k_{3r} = 0$). In [^{11}C]PIB, the gray matter of the cerebellum is usually used as a reference tissue for input function [14]. We apply the one-tissue compartment two-parameter (K_1, k_2) model (2P model) to the reference tissue.

Working equation for 3P++ analysis

The working equation for the 3P++ analysis has been reported [15]:

$$\begin{aligned} C_t(t) &= R_1\left[\delta(t) + \frac{k_{2r}k_3}{k_2+k_3} + \left(k_{2r} - k_2 - \frac{k_{2r}k_3}{k_2+k_3}\right)e^{-(k_2+k_3)t}\right] \otimes C_r(t) \\ &= R_1 C_r(t) + \frac{R_1 k_{2r} k_3}{k_2+k_3}\int_0^t C_r(\tau)d\tau - \frac{R_1 k_2 (k_2+k_3-k_{2r})}{k_2+k_3} \\ &\quad \times \int_0^t e^{-(k_2+k_3)(t-\tau)} C_r(\tau)d\tau, \end{aligned} \tag{1}$$

where $C_t(t)$ is the radioactivity concentration in the target tissue and $C_r(t)$ is that in the reference tissue; k_{2r} is the k_2 in the reference tissue and $\otimes$ is the convolution integral. The rate of tracer penetration into the target tissue is obtained as the relative value R_1, which is the ratio of target K_1 to reference K_1.

Clinical PET study

Human subjects

Two groups of subjects, a normal control (NC) group and an Alzheimer's disease (AD) group, participated in

the current study with written informed consent. The NC group consisted of 15 healthy subjects (age ranging from 48 to 90 years, 66.7 ± 11.5 years (mean ± SD); eight males and seven females) without a history of central nervous system diseases or psychiatric disorders, and the AD group consisted of 15 patients (ages 55 to 85, 68.9 ± 9.6 years; four males and 11 females) diagnosed as probable AD according to the criteria of the National Institute of Neurological and Communication Disorders, Alzheimer's Disease and Related Disorders Association [16]. The study was approved by the Institutional Review Board of the National Institute of Radiological Sciences.

Radiochemical synthesis

[^{11}C]PIB was synthesized by the reaction of 2-(4′-aminophenyl)-6-hydroxy-benzothiazole and [^{11}C]methyl triflate [17]. The product had radiochemical purity greater than 95.4%. Specific activity was in the range of 56.3 to 285.3 GBq/μmol.

PET scan protocol

PET images were acquired with a Siemens ECAT EXACT HR + scanner (CTI PET systems, Inc., Knoxville, TN, USA) with an axial field of view of 155 mm, providing 63 contiguous 2.46-mm slices with 5.6-mm transaxial and 5.4-mm axial resolution. After a 10-min transmission scan for tissue attenuation correction, infusion of [^{11}C]PIB (about 370 MBq in 5 mL for 1 min) began. A PET scan in 3D mode was started after the arrival of tracer to the brain (approximately 30 s after the beginning of tracer infusion). The dynamic scans consisted of 19 frames (3 × 20 s, 3 × 40 s, 1 × 1 min, 2 × 3 min, 5 × 6 min, and 5 × 10 min) with the total scan duration of 90 min. All data processing and image reconstruction were performed using standard Siemens software, which included scatter correction, randoms, and dead time correction.

Region-of-interest delineation

Region-of-interest (ROI) analysis was performed using the PMOD software package (PMOD version 3.2; Technologies Ltd., Adliswil, Switzerland). The [^{11}C]PIB PET images were co-registered to T_1 weighted images in each subject. The following 15 ROIs were drawn manually on T_1 weighted images: frontal, mesial temporal, lateral temporal, parietal, occipital, anterior cingulate, and posterior cingulate cortices in both hemispheres as well as the reference tissue (gray matter of cerebellum). ROIs were transferred to co-registered [^{11}C]PIB PET images, and time-activity curves (TACs) were obtained in those brain regions.

Input function measurement

During PET scan, arterial blood was collected from radial artery, starting 6 s (transit delay at the blood sampling site) after the beginning of PET scan to 85 min post injection (10 × 10 s, 1 × 30 s, 9 × 2 min, 6 × 10 min, and 1 × 5 min; 27 samples). Radioactive metabolites were analyzed by a radio-thin layer chromatography (TLC) method [12], with a TLC-developing solvent (ethyl acetate/*n*-hexane = 2:1 vols). The metabolite-corrected radioactivity as well as total radioactivity in blood plasma was fitted to a mono-exponential saturation function during infusion (0 to 1 min) and the sum of three-exponential functions after the end of infusion (1 to 85 min) [12].

4P and 3P + analyses (arterial-plasma input)

Brain regional TACs were analyzed by the weighted NLS method under positive constraint of all k_i with metabolite-corrected input function to afford K_1 to k_4 estimates in 4P analysis (scan time of 90 min) and K_1 to k_3 estimates in 3P + analysis (40 min). Correction was made for blood-pool (5%) radioactivity in brain tissue [14]. Custom software operating in IDL software (version 6.0; Jicoux Datasystems, Inc., Tokyo, Japan) environment was used for the compartment model analysis.

3P++ analysis (reference tissue input)

For successful convergence in NLS optimization using Equation 1, we fixed k_{2r} to 0.178/min (mean cerebellar k_2 value by 40-min 3P + analysis; $N = 30$; SD = 0.034). Based on Equation 1 and cerebellar TAC with a fixed k_{2r} value, the time-integral of $C_r(t)$ (the second term on the right side of Equation 1) and the convolution integral (the third term) were calculated numerically without data interpolation for each scan mid-times during 0 to 40 min, and the three parameters R_1, k_2, and k_3 were estimated.

Simulation study

Generation of error-added TACs for Monte Carlo simulation

The error-free, baseline TACs (19 frames/90 min) simulating the target ROI of the NC and AD subjects were generated by using the 4P model with parameter set (K_1 = 0.180 mL/g/min, k_2 = 0.180/min, k_3 = 0.018 and 0.036/min for the NC and AD subjects, respectively, and k_4 = 0.018/min; typical values for [^{11}C]PIB) and averaged (N = 20) input function of [^{11}C]PIB. The reference ROI was the same between NC and AD subjects and was generated by using the 2P model with parameter set (K_1 = 0.180 mL/g/min, k_2 = 0.180/min) and the same input function as above. The error-added TACs for simulation were generated according to the following formula [18]:

$$\text{Error-added } C_i = C_i + \text{Rand} \times \sigma(C_i),$$
$$\sigma(C_i) = \varepsilon\sqrt{\frac{C_i}{\Delta t_i \times \exp(-\lambda t_i)}}, \quad (2)$$

where C_i is noise-free simulated radioactivity concentration at frame number i, Rand is a random number from a Gaussian distribution with a mean 0 and variance 1, ε is a

scaling factor that determines the noise level, Δt_i is scan duration of frame number i, t_i is mid-scan time of frame number i, and λ is ^{11}C decay constant. In all Monte Carlo simulations, a data set of 100 noise-added TACs was analyzed with weighted NLS, using a relative weight w_i:

$$w_i = \text{constant} \times \frac{\Delta t_i \times \exp(-\lambda t_i)}{C_i}. \quad (3)$$

Effects of PET noise on 4P, 3P+, and 3P++ analyses

Five levels of PET noise (0.025, 0.05, 0.1, 0.2, and 0.3; ε in Equation 2, relative values empirically determined) were added to the baseline TACs of the target ROI of the NC subjects. From 100 error-added TACs for each PET noise level, 100 k_3 values were estimated using 90-min 4P, 40-min 3P+, and 3P++ analyses. Coefficient-of-variation (CV) of k_3 was calculated as CV (%) = (SD/mean) × 100. In the following simulations, the PET noise was fixed at 0.1.

Effects of K_1 change in target ROI on 4P, 3P+, and 3P++ analyses

Simulated target TACs were generated by 4P model with five different K_1 values (0.12, 0.15, 0.18, 0.21, and 0.24 mL/g/min) and fixed k_3 (0.018/min) and k_4 (0.018/min). The value of K_1/k_2 was fixed at 1. The range of K_1 was determined with clinically measured K_1 for [^{11}C]PIB (0.177 ± 0.31 in NC group and 0.168 ± 0.30 in AD group; 90-min 4P analysis). Reference TAC was the same as baseline reference TAC. The k_3 bias in 90-min 4P, 40-min 3P+, and 3P++ analyses relative to the true k_3 (0.018/min) was calculated as bias (%) = (estimated k_3/true k_3 − 1) × 100.

Effects of k_2 or k_3 change in reference ROI on 3P++ analysis

In 3P++ analysis, k_{3r} was assumed to be 0 and k_{2r} was fixed as an empirical constant. The effects of k_{2r} or k_{3r} change were investigated as follows. The error-added target TACs were generated by 4P model with two different k_3 values (0.018/min for NC and 0.036/min for AD); other parameters were the same as the baseline target TAC. The error-added reference TACs were generated by 2P model with five different k_2 (0.12, 0.15, 0.18, 0.21, and 0.24/min) and fixed K_1 values (0.18 mL/g/min). Another set of simulated reference TACs was generated by 3P model (not 2P model) with five different k_3 (0, 0.002, 0.004, 0.006, and 0.008/min) and fixed K_1 (0.18 mL/g/min) and k_2 (0.18/min). The k_3 bias in 3P++ analysis was expressed relative to 3P + analysis as bias (%) = (3P++ k_3/3P + k_3 − 1) × 100.

Although k_{3r} was assumed to be 0 in Equation 1, each subject may have different k_{3r} values that deviated from 0. In simulations to investigate the effect of the individual k_{3r} variation on 3P++ analysis, we defined the k_3 value empirically corrected for nonzero k_{3r} as follows: $k_3' = k_3 + k_{3r}$, where k_3 is the k_3 estimate of target ROI by 3P++ analysis and k_{3r} is the k_3 estimate of reference ROI by 3P + analysis (true reference k_3). Bias in 3P++ k_3' relative to 3P + k_3 was compared with the bias in 3P++ k_3 to 3P + k_3.

Results

Goodness of model fits in 3P++ analysis

Figure 1A shows an example of the curve fitting of [^{11}C]PIB cerebellar TAC data to the 2P model, where a good fit is seen during 0 to 40 min after tracer injection. Figure 1B shows the fits of cerebral cortical TAC data (0 to 40 min) to the 3P + and 3P++ models. The goodness-of-fit by 3P++ model (reference tissue input) is almost indistinguishable from that by 3P + model (arterial-plasma input). Kinetic parameters (K_1 = 0.161 mL/g/min, k_2 = 0.167/min and

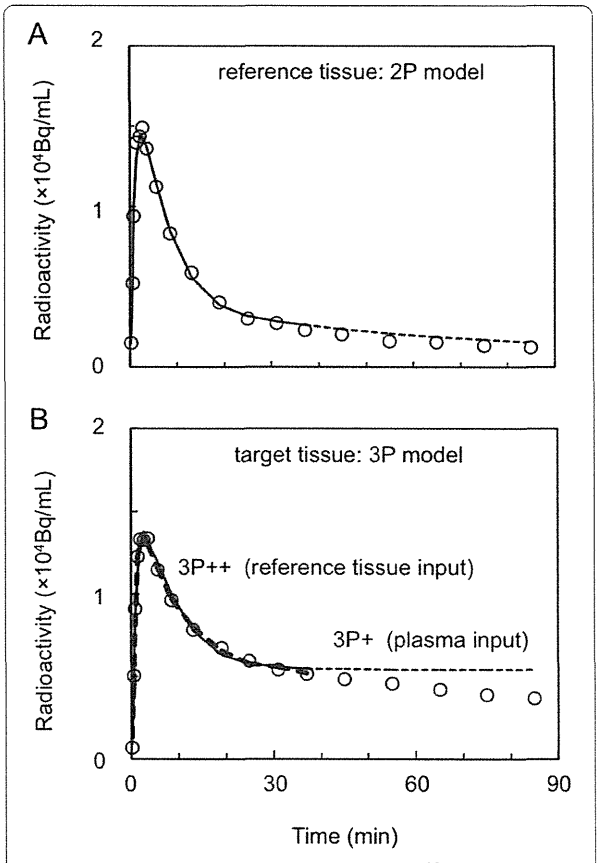

Figure 1 Reference and target tissue TACs in [^{11}C]PIB PET. (A) Cerebellar (reference tissue) data (open circle) up to 90 min in one AD subject and the fit of 40-min data to the 2P model (solid line). **(B)** Cerebral cortical (target tissue) data (open circle) in the same subject and the fits of 40-min data to the 3P model with arterial-plasma input (3P + analysis; solid line) or reference tissue input (3P++ analysis; dashed line). The dotted lines in **(A)** and **(B)** indicate the extension of the solid line from 40 to 90 min.

k_3 = 0.015/min) were estimated in 3P + analysis and R_1 = 0.897, k_2 = 0.158/min and k_3 = 0.011/min in 3P++ analysis.

Intra-subject k_3 correlation

Figure 2A is an example of the intra-subject k_3 correlation between 40-min 3P + (*X*-axis) and 3P++ (*Y*-axis) analyses, where the k_3 values of 15 ROIs, including the cerebellum (reference tissue in 3P++ analysis) from one particular NC subject or one particular AD subject, are shown. The regression lines and the coefficients of determination are $Y = 0.845X - 0.006$ ($r^2 = 0.972$) for the NC subject and $Y = 0.655X - 0.004$ ($r^2 = 0.982$) for the AD subject. Cerebellar k_3 values for both subjects are naturally calculated to be 0 in the 3P++ analysis. The slopes of the regression lines indicate the presence of negative bias in the 3P++ against the 3P + analysis.

Figure 2B shows the k_3 correlation between 90-min 4P (*X*-axis) and 40-min 3P++ (*Y*-axis) analyses in the same subjects. The regression lines are $Y = 0.590X - 0.005$ (r^2 = 0.953) for the NC subject and $Y = 0.338X + 0.000$ (r^2 = 0.907) for the AD subject. When the cerebellar data ($X = 0.008$, $Y = 0.000$) was removed from calculation for the AD subject, the regression line became $Y = 0.295X - 0.002$ with slightly larger r^2 (0.935; not shown in the figure). The slopes of the regression lines show that k_3 bias in 3P++ against 4P analysis is larger than that against 3P + analysis.

Inter-subject k_3 correlation

Figure 3A shows an example of the inter-subject k_3 correlation, where k_3 values for the left lateral temporal cortex from 30 subjects (15 NC + 15 AD) are compared between 40-min 3P + (*X*-axis) and 3P++ (*Y*-axis) analyses. The regression lines are $Y = 0.461X - 0.001$ (r^2 = 0.739) for all 30 subjects, $Y = 0.178X + 0.000$ ($r^2 = 0.151$) for the NC group alone, and $Y = 0.286X + 0.003$ (r^2 = 0.411) for the AD group alone; the latter two lines are not shown in the figure. The slopes of the regression lines also indicate the presence of negative biases in 3P++ against 3P + analysis.

Figure 3B shows the inter-subject correlation of left lateral temporal k_3 between 90-min 4P (*X*-axis) and 40-min 3P++ (*Y*-axis) analyses, where the regression line is $Y = 0.225X + 0.000$ ($r^2 = 0.711$) for all subjects. The lines of $Y = 0.090X + 0.001$ ($r^2 = 0.122$) for the NC group alone and $Y = 0.135X + 0.005$ ($r^2 = 0.513$) for the AD group alone were also calculated. The slopes of the regression lines show larger negative k_3 biases in 3P++ against 4P analysis than that shown in Figure 3A. The results in other cerebral regions were essentially the same as those in the left lateral temporal cortex.

Simulation on the effects of PET noise on k_3 CV

Figure 4 compares the noise sensitivity of k_3 estimates among the 90-min 4P, 40-min 3P+, and 3P++ analyses. In all three analyses, the k_3 CVs increased as the PET error became larger. The k_3 CV in 3P++ analysis was comparable to that in 3P + analysis and lower than that in 4P analysis; for example, k_3 CVs at 0.1 of noise level were 6.6% in 3P++, 7.0% in 3P+, and 11.4% in 4P analyses.

Simulation on the effects of target K_1 change on k_3 bias

Figure 5 shows the effects of K_1 change in the target ROI on the k_3 biases in the 90-min 4P, 40-min 3P+, and 3P++ analyses. The 4P analysis remained almost bias-free (+0.6%) within K_1 from 0.12 to 0.24 mL/g/min. 3P + and 3P++ analyses showed larger negative biases (−33% to −34% bias in 3P + and −33% to −35% bias in 3P++) compared with 4P analysis. Although 3P++ analysis showed slightly larger k_3 bias than 3P + analysis

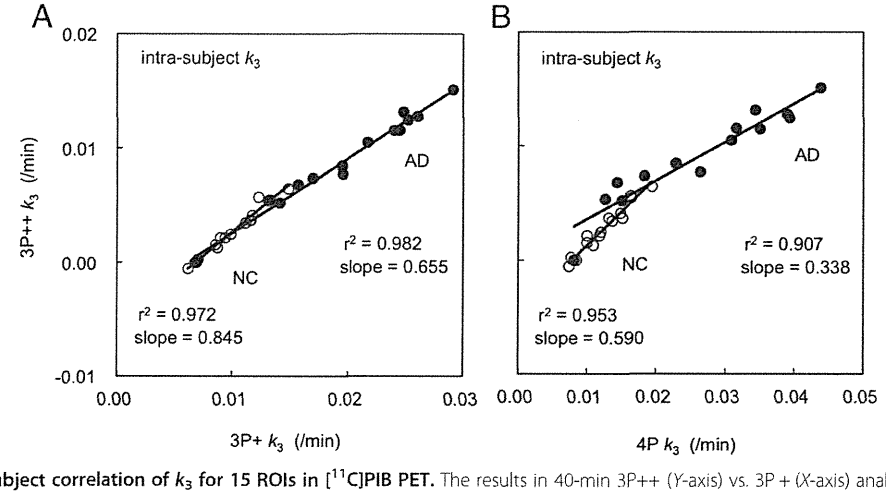

Figure 2 Intra-subject correlation of k_3 for 15 ROIs in [^{11}C]PIB PET. The results in 40-min 3P++ (*Y*-axis) vs. 3P + (*X*-axis) analyses **(A)** and 40-min 3P++ vs. 90-min 4P analyses **(B)** with one NC subject (open circle) and one AD subject (closed circle) are shown.

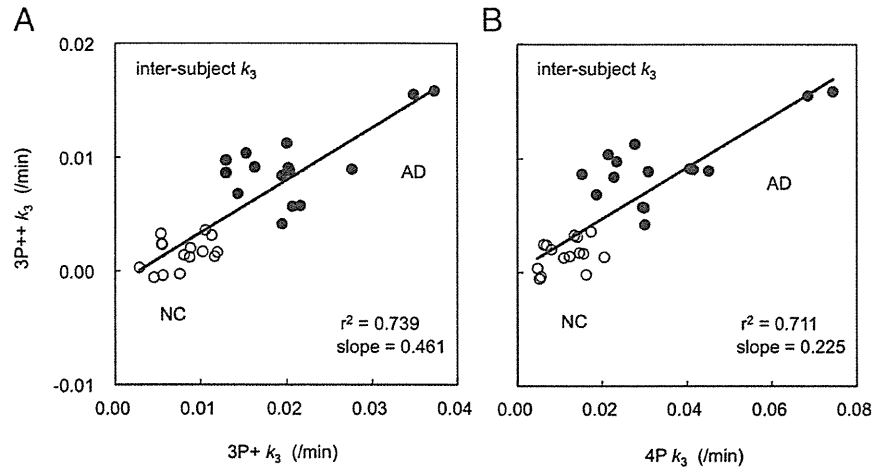

Figure 3 Inter-subject correlations of left lateral temporal k_3 in [^{11}C]PIB PET. The results in 40-min 3P++ (*Y*-axis) vs. 3P + (*X*-axis) analyses **(A)** and 40-min 3P++ vs. 90-min 4P analyses **(B)** with 30 subjects (15 NC, open circle; 15 AD, closed circle) are shown.

when K_1 was low (0.12 mL/g/min), k_3 bias in 3P++ analysis was almost the same as 3P + analysis.

Simulation on the effects of k_{2r} change on 3P++ analysis

In 3P++ analysis (Equation 1), k_{2r} was fixed at 0.178/min, though k_{2r} was not always the same among subjects (CV = 19%). Figure 6 shows the effects of individual k_{2r} change in 40-min 3P++ analysis. When k_{2r} was equal to the fixed value (0.18/min), 3P++ analysis was bias-free, relative to 3P + analysis. However, when k_{2r} was different from the fixed value, 3P++ analysis showed a negative k_3 bias relative to 3P + k_3. The k_{2r} effects were similar between NC ROI (k_3 = 0.018/min) and AD ROI (k_3 = 0.036/min); for example, the biases were −14.1% for NC and −12.1% for AD at k_{2r} = 0.12/min and −14.1% for NC and −11.3% for AD at k_{2r} = 0.24/min.

Simulation on the effects of k_{3r} change on 3P++ analysis

In 3P++ analysis we assume that k_{3r} = 0, that is, specific binding is negligible in the reference tissue. However, in all subjects examined, this assumption did not hold: the k_{3r} values in 40-min 3P + analysis were 0.008 ± 0.004/min in the AD group, 0.007 ± 0.002/min in the NC group, and 0.007 ± 0.003/min in the AD + NC group.

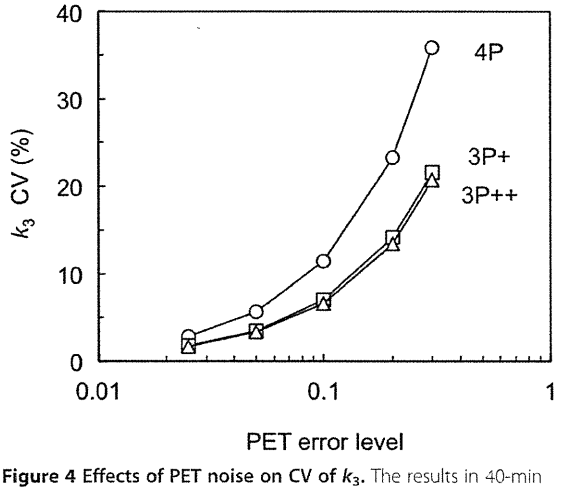

Figure 4 Effects of PET noise on CV of k_3. The results in 40-min 3P++ (open triangle), 40-min 3P + (open square), and 90-min 4P (open circle) analyses are shown. Five different PET noises (0.025 to 0.3) were added to the [^{11}C]PIB baseline TACs of the target ROI of the NC subjects. CV of k_3 was calculated from 100 k_3 estimates as CV (%) = (SD/mean) × 100.

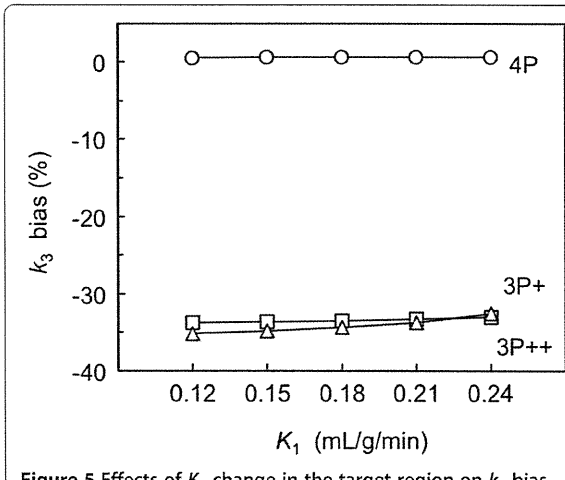

Figure 5 Effects of K_1 change in the target region on k_3 bias. The results in 40-min 3P++ (open triangle), 40-min 3P + (open square) and 90-min 4P (open circle) analyses are shown. Simulated target TACs were generated by 4P model with five different K_1 values (0.12 to 0.24 mL/g/min). The k_3 bias was calculated as bias (%) = (estimated k_3/true k_3 − 1) × 100.

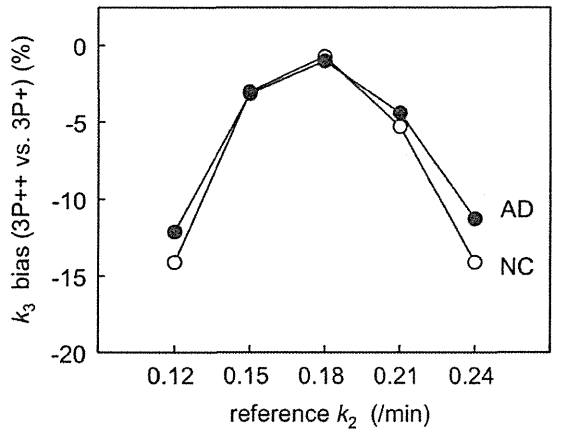

Figure 6 Effects of k_2 change in the reference region on k_3 bias in 40-min 3P++ analysis. Simulated target TACs were generated by 4P model with two different k_3 values (0.018/min for NC, open circle; 0.036/min for AD, closed circle). Simulated reference TACs were generated by 2P model with five different k_2 values (0.12 to 0.24/min). The k_3 bias in 3P++ analysis was expressed relative to 3P + analysis as bias (%) = (3P++ k_3/3P + k_3 − 1) × 100.

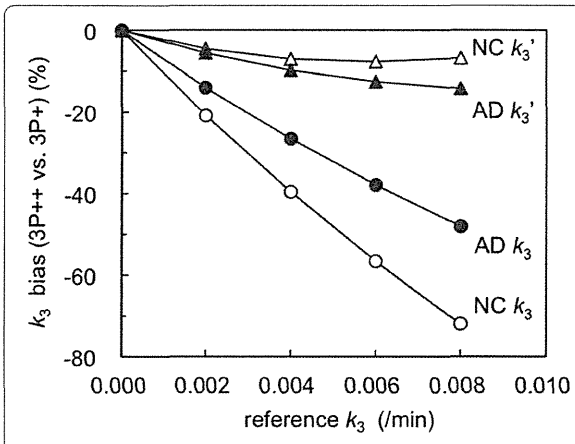

Figure 7 Effects of k_3 change in the reference region on k_3 bias in 40-min 3P++ analysis. Simulated target TACs were generated by 4P model with two different k_3 values (0.018/min for NC, open circle; 0.036/min for AD, closed circle). Simulated reference TACs were generated by 3P model with five different k_3 values (0 to 0.008/min). The k_3 bias in 3P++ analysis was expressed relative to 3P + analysis as bias (%) = (3P++ k_3/3P + k_3 − 1) × 100. Effects on bias in 3P++ k_3' relative to 3P + k_3 are also shown (NC, open triangle; AD, closed triangle), where 3P++ k_3' was calculated as (3P++ k_3') = (3P++ k_3) + reference k_3.

Figure 7 shows the effects of individual k_{3r} change (0 to 0.008/min) on 40-min 3P++ analysis. When k_{3r} was 0, 3P++ analysis was bias-free, relative to 3P + analysis. The k_3 biases (negative biases) increased as k_{3r} increased: −38% for NC and −27% for AD at k_{3r} = 0.004/min and −70% for NC and −48% for AD at k_{3r} = 0.008/min. The NC ROI (k_3 = 0.018/min) showed larger biases than the AD ROI (k_3 = 0.036/min). Figure 7 also shows the results of the simulation study on the relationship between 3P++ k_3' and 3P + k_3, where 3P++ k_3 was empirically corrected with individual k_{3r}. In this case, negative bias in 3P++ k_3' was significantly decreased compared to that in 3P++ k_3; for example, bias was decreased from −70% to −7% for NC, and from −48% to −15% for AD at k_{3r} = 0.008/min.

Figure 8 shows the correlation between 3P++ k_3' and 3P + k_3 using the same data as in Figure 3A, where 3P++ k_3 in Figure 3A was replaced by 3P++ k_3'. The regression line was $Y = 0.678X + 0.003$ ($r^2 = 0.975$) for all subjects, where X = 3P + k_3 and Y = 3P++ k_3'. The lines of $Y = 0.798X + 0.002$ ($r^2 = 0.897$) for the NC group alone and $Y = 0.620X + 0.004$ ($r^2 = 0.960$) for the AD group alone were also calculated. The determination coefficient was increased by this correction from 0.739 to 0.975. The slope of the regression line was also increased from 0.461 (Figure 3A) to 0.678 (Figure 8), which showed the reduction of negative bias in 3P++ analysis.

Discussion

Theoretical basis and merits of 3P++ analysis

The previous 3P + analysis allowed for estimating k_3 of moderately reversible ligands, where the 3P model was applied to early-phase (up to 30 to 40 min) PET data with arterial input function [13]. It was reported that when the 3P model was applied to 60-min PET scan data from [^{11}C]PIB (k_4 = 0.018/min) as a moderately reversible ligand, only a poor model fit was obtained [19]. Previous simulation studies on [^{11}C]PIB using information

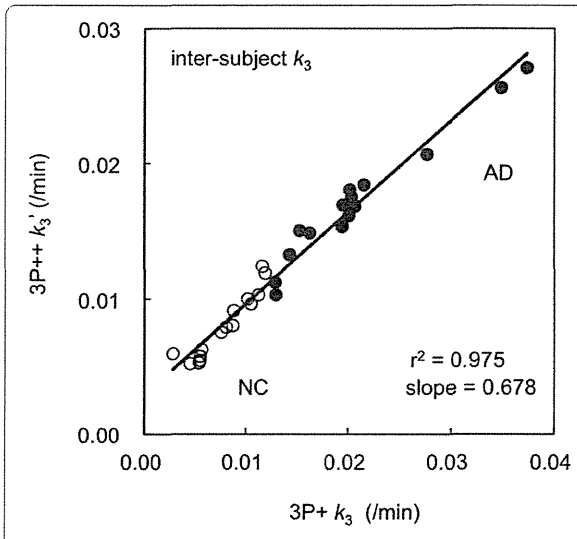

Figure 8 Inter-subject correlation of left lateral temporal k_3 in [^{11}C]PIB PET. The result in 40-min 3P++ (*Y*-axis) vs. 3P + (*X*-axis) analyses with 30 subjects (15 NC, open circle; 15 AD, closed circle) is shown. The k_3 estimates were empirically corrected as (3P++ k_3') = (3P++ k_3) + (individual cerebellar k_3 by 3P+).

density theory suggested that scan time reduction to 40 min would be necessary to obtain a good fit to the 3P model [13].

When 3P + or 3P++ analysis can be applied to a ligand, such ligand is specified as a moderately reversible ligand. This applicability is determined by the information function curves of k_3 and k_4 [13], and thus is dependent on the scan time as well as k_3 and k_4 values of the ligand in a ROI. Differentiation of a moderately reversible ligand from general reversible ligands is somewhat arbitrary, though we conveniently defined this with the k_4 value (≤0.03/min) in this study.

In the present study, the 3P + plasma input model was extended to the 3P++ reference tissue input model. The 3P++ analysis has three merits over previous methods. First, the PET scan time is short, usually less than 40 min, which may be important in PET studies with elderly or demented subjects. Secondly, the target parameter k_3 can be isolated from the other model parameters. Thirdly, neither arterial cannulation nor labor-intensive measurements of labeled metabolites are required.

One of the conventional models for the estimation of binding of [^{11}C]PIB is the Logan plot analysis [2], which employs data of long duration (more than 60 min). Noninvasive Logan analysis (distribution volume ratio) [6] requires late-phase (equilibrium-phase) PET data, whereas late-phase data are not necessary for 3P++ analysis. In the noninvasive Logan model or simplified reference tissue model [8], the K_1-to-k_2 ratio in the target and reference tissues is assumed to be equal. 3P++ analysis does not require such an assumption. Since 3P++ analysis is a kind of irreversible-model analysis, K_1 (R_1) and k_3 can be independently estimated (k_2 must be fixed to a certain constant).

Noise sensitivity of 3P++ analysis

Loss of PET data in short-scan 3P++ and 3P + analyses might be considered to deteriorate the precision of the k_3 estimate. In the present simulation for noise sensitivity, k_3 CV values in 40-min 3P++ and 3P + analyses were lower than (almost three fifths of) that in 90-min 4P analysis (Figure 4), which was in accordance with the previous report [13]. It is considered that the loss of PET data may be compensated for by the reduction in the number of free parameters from four in the 4P model to three in the 3P + and 3P++ models.

K_1 effect on 3P++ analysis

In the K_1 simulation, the stableness of k_3 estimation in changes of cerebral blood flow was investigated. The magnitudes of k_3 bias were independent of the K_1 change, ranging from 0.12 to 0.24 mL/g/min, in 3P++, 3P+, and 4P analyses (Figure 5). The 3P++ as well as 3P + and 4P analyses were less affected by K_1, which is owing to the capability of isolating the k_3 estimation. The 40-min 3P + analysis showed −33% k_3 bias relative to 90-min 4P analysis, which is in accordance with the previous report [13]. In this K_1 simulation, 3P++ k_3 showed negligible bias relative to 3P + k_3. These results suggested that in 3P++ analysis, the effects of ignoring vascular volume as well as numerical integration error due to discrete time points were not significant.

Causes of negative k_3 bias in 3P++ analysis

Firstly, the k_3 bias in 3P++ analysis originates from 3P model approximation. Our previous simulation study [13] showed that the 3P + analysis with 28-min scan had large negative k_3 bias relative to 4P analysis with 90-min scan; for example, there was about −22% to −24% bias to true k_3 (4P k_3) ranging from 0.01 to 0.04/min including NC and AD k_3. 3P++ analysis showed further negative k_3 bias relative to 3P + analysis due to the following two reasons.

Secondly, the bias is due to individual k_{2r} change from the fixed value in Equation 1. In 3P++ analysis, we also assumed that k_2 in the reference tissue was constant and was fixed at 0.178/min, which was the average k_2 value with the 3P + model. In simulation, negative k_3 bias was predicted when k_{2r} was larger or smaller than fixed k_2 (Figure 6). Each subject in the NC and AD groups had different k_2 values in the reference tissue, and it is considered that such biological variance as for reference tissue may result in a negative k_3 bias in 3P++ analysis, relative to 3P + analysis for [^{11}C]PIB.

Thirdly, the bias is due to the discrepancy between the model assumption and the actual reference ROI. The basic assumption (assumption 3) in 3P++ analysis is $k_{3r} = 0$. The working equation of 3P++ analysis (Equation 1) is derived under this assumption, and reference k_3 is naturally calculated to be 0. However, in 3P + analysis with [^{11}C]PIB, the cerebellum showed nonzero k_3 (0.007 ± 0.003/min in all 30 subjects). Thus, 3P++ k_3 is expected to be underestimated. Simulation studies showed that 3P++ analysis was bias-free for ideal reference with zero k_3 and that k_3 bias became larger as k_{3r} increased (Figure 7). When k_3 was replaced by k_3', negative bias was significantly decreased in the simulation (Figure 7), as well as the slope of the regression line between 3P++ and 3P + analyses being increased from 0.461 (Figure 3A) to 0.678 (Figure 8), which also suggested that nonzero k_{3r} caused underestimation of 3P++ k_3.

Correlation of k_3 between 3P++ and 3P + analyses

Strong intra-subject k_3 correlation was shown between 3P++ and 3P + analyses, and the rank-order of k_3 was almost the same between the two analyses (Figure 2A), suggesting the stability of both 3P++ and 3P + analyses.

The inter-subject k_3 correlation (r^2; Figure 3A) was significantly lower than the intra-subject correlation (Figure 2A). Such a lower inter-subject k_3 correlation

can be partly explained by the sample variance of cerebellar k_3. In order to explain this, k_3' was calculated for each subject. When k_3 was replaced by k_3', the determination coefficient between 3P++ and 3P + analyses was increased from 0.739 (Figure 3A) to 0.975 (Figure 8); the latter is comparable to r^2 of the intra-subject k_3 correlation (0.982; Figure 2A).

Such an estimation of parameter k_3' is not always practical, as 3P + analysis with arterial input function is necessary for individual cerebellar k_3 estimation. However, these results suggest that the lower r^2 in the inter-subject correlation compared with the intra-subject correlation is due to the sample variance of cerebellar k_3 and that 3P++ analysis itself is robust, as far as the reference is ideal.

Practically, the use of mean k_{3r} may be meaningful. When target k_3 is empirically corrected as corrected k_3 = estimated k_3 + mean cerebellar k_3, the absolute bias in target k_3 would decrease. However, the precision of target k_3 would not necessarily be improved owing to the variance of individual k_{3r}.

In addition to the nonzero effect of k_{3r}, inter-subject variation of k_{2r} from the fixed value (k_2 = 0.178/min) may also produce individually different k_3 bias in 3P++ analysis, resulting in lower inter-subject k_3 correlation between 3P + and 3P++ analyses.

Limitations of 3P++ analysis

When 3P++ analysis was applied to [^{11}C]PIB as an example of moderately reversible ligands, a somewhat lower inter-subject k_3 correlation (r^2 = 0.739 or 0.711; Figure 3A or Figure 3B) was shown between the 3P++ and 3P + or 4P analyses, respectively, across a k_3 range including NC and AD (3P + k_3, 0.004 to 0.040/min). The rank order of 3P++ k_3 also differed considerably from 3P + k_3 or 4P k_3. These results were mainly due to nonzero k_{3r} and the sample variance of both k_{2r} and k_{3r} as described above. The negative k_3 bias (3P++ vs. 3P+) was larger in NC ROI (−70%) than in AD ROI (−48%) when k_{3r} = 0.008/min (Figure 7). The previous report showed that the difference in k_3 bias (28-min 3P + vs. 90-min 4P) was small between NC ROI (−23%) and AD ROI (−24%) [13]. Therefore, the k_3 value in 3P++ analysis may be somewhat underestimated in the ROI with lower amyloid deposition compared to 3P + or 4P analysis.

In [^{11}C]PIB PET, 3P++ analysis may be inadequate for inter-subject k_3 comparison and useful only for intra-subject (inter-ROI) comparison or pre- vs. post-comparison in the same subject. 3P++ analysis would be more suitable for such reversible ligands that have moderate k_4 and reference tissue without specific binding.

Conclusions

The 3P++ analysis is a k_3 estimation method for moderately reversible PET ligands with a short scan time such as 40 min and without arterial blood sampling. Although the applicability of 3P++ method to [^{11}C]PIB PET may be restricted to intra-subject comparison, 3P++ analysis itself is robust. The 3P++ method would be useful for PET study with non-highly reversible ligands, as far as the reference tissue without specific binding is available.

Competing interests

The authors declare that they have no competing interests.

Authors' contributions

KS participated in clinical PET study and the simulation study, and drafted the manuscript. KF conceived of the study, participated in the simulation study, and helped to draft the manuscript. HS (Shinotoh), HS (Shimada), SH, and NT participated in clinical PET study and contributed to the discussion. TS, TI, and HI supervised the design and coordination of the study. All authors read and approved the final manuscript.

Acknowledgements

The authors thank the production team staff for the production of isotopes and the PET operation staff for the acquisition of PET images.

Author details

[1]Molecular Imaging Center, National Institute of Radiological Sciences, 4-9-1 Anagawa, Inage-ku, Chiba 260-8555, Japan. [2]Department of Psychiatry, Teikyo University Chiba Medical Center, 3426-3 Anesaki, Ichihara-shi, Chiba 299-0111, Japan. [3]Neurology Chiba Clinic, 1-2-12 Benten, Chuo-ku, Chiba 260-0045, Japan. [4]Section for Human Neurophysiology, Research Center for Frontier Medical Engineering, Chiba University, 1-33 Yayoi-cho, Inage-ku, Chiba 263-8522, Japan. [5]Department of Neurology, Graduate School of Medicine, Chiba University, 1-8-1 Inohana, Chuo-ku, Chiba 260-8677, Japan. [6]Bureau of Social Welfare and Public Health, Tokyo Metropolitan Government, 2-8-1 Nishi-shinjuku, Shinjuku-ku, Tokyo 163-8001, Japan.

Received: 4 October 2013 Accepted: 6 November 2013
Published: 16 November 2013

References

1. Mintun MA, Raichle ME, Kilbourn MR, Wooten GF, Welch MJ: **A quantitative model for the in vivo assessment of drug binding sites with positron emission tomography.** *Ann Neurol* 1984, **15**:217–227.
2. Logan J, Fowler JS, Volkow ND, Wolf AP, Dewey SL, Schlyer DJ, MacGregor RR, Hitzemann R, Bendriem B, Gatley SF, Christman DR: **Graphical analysis of reversible radioligand binding from time-activity measurements applied to [N-^{11}C-methyl]-(-)-cocaine PET studies in human subjects.** *J Cereb Blood Flow Metab* 1990, **10**:740–747.
3. Hume SP, Myers R, Bloomfield PM, Opacka-Juffry J, Cremer JE, Ahier RG, Luthra SK, Brooks DJ, Lammertsma AA: **Quantification of carbon-11-labeled racropride in rat striatum using positron emission tomography.** *Synapse* 1992, **12**:47–54.
4. Innis RB, Cunningham VJ, Delforge J, Fujita M, Gjedde A, Gunn RN, Holden J, Houle S, Huang SC, Ichise M, Iida H, Ito H, Kimura Y, Koeppe RA, Knudsen GM, Knuuti J, Lammertsma AA, Laruelle M, Logan J, Maguire RP, Mintun MA, Morris ED, Parsey R, Price JC, Slifstein M, Sossi V, Suhara T, Votaw JR, Wong DF, Carson RE: **Consensus nomenclature for in vivo imaging of reversibly binding radioligands.** *J Cereb Blood Flow Metab* 2007, **27**:1533–1539.
5. Ichise M, Ballinger JR, Golan H, Vines D, Luong A, Tsai S, Kung HF: **Noninvasive quantification of dopamine D2 receptors with iodine-123-IBF SPECT.** *J Nucl Med* 1996, **37**:513–520.
6. Lammertsma AA, Hume SP: **Simplified reference tissue model for PET receptor studies.** *Neuroimage* 1996, **4**:153–158.
7. Lammertsma AA, Bench CJ, Hume SP, Osman S, Gunn K, Brooks DJ, Frackowiak RSJ: **Comparison of methods for analysis of clinical [^{11}C] raclopride studies.** *J Cereb Blood Flow Metab* 1996, **16**:42–52.
8. Logan J, Fowler JS, Volkow ND, Wang GJ, Ding YS, Alexoff DL: **Distribution volume ratios without blood sampling from graphical analysis of PET data.** *J Cereb Blood Flow Metab* 1996, **16**:834–840.
9. Watabe H, Carson RE, Iida H: **The reference tissue model: three compartments for the reference region [abstract].** *Neuroimage* 2000, **11**:S12.

10. Wu Y, Carson RE: **Noise reduction in the simplified reference tissue model for neuroreceptor functional imaging.** *J Cereb Blood Flow Metab* 2002, **22**:1440–1452.
11. Koeppe RA, Frey KA, Snyder SE, Meyer P, Kilbourn MR, Kuhl DE: **Kinetic modeling of N-[^{11}C]methylpiperidin-4-yl propionate: alternatives for analysis of an irreversible positron emission tomography tracer for measurement of acetylcholinesterase activity in human brain.** *J Cereb Blood Flow Metab* 1999, **19**:1150–1163.
12. Namba H, Iyo M, Fukushi K, Shinotoh H, Nagatsuka S, Suhara T, Sudo Y, Suzuki K, Irie T: **Human cerebral acetylcholinesterase activity measured with positron emission tomography: procedure, normal values and effect of age.** *Eur J Nucl Med* 1999, **26**:135–143.
13. Sato K, Fukushi K, Shinotoh H, Shimada H, Tanaka N, Hirano S, Irie T: **A short-scan method for k_3 estimation with moderately reversible PET ligands: application of irreversible model to early-phase PET data.** *Neuroimage* 2012, **59**:3149–3158.
14. Price JC, Klunk WE, Lopresti BJ, Lu X, Hoge JA, Ziolko SK, Holt DP, Meltzer CC, DeKosky ST, Mathis CA: **Kinetic modeling of amyloid binding in humans using PET imaging and Pittsburgh Compound-B.** *J Cereb Blood Flow Metab* 2005, **25**:1528–1547.
15. Gunn RN, Gunn SR, Cunningham VJ: **Positron emission tomography compartmental models.** *J Cereb Blood Flow Metab* 2001, **21**:635–652.
16. McKhann G, Drachman D, Folstein M, Katzman R, Price D, Stadlan EM: **Clinical diagnosis of Alzheimer's disease: report of the NINCDS-ADRDA work group under the auspices of Department of Health and Human Services Task Force on Alzheimer's Disease.** *Neurology* 1984, **34**:939–944.
17. Mathis CA, Wang Y, Holt DP, Huang G-F, Debnath ML: **Synthesis and evaluation of ^{11}C-labeled 6-substituted 2-aryl benzothiazoles as amyloid imaging agents.** *J Med Chem* 2003, **46**:2740–2754.
18. Logan J, Fowler JS, Volkow ND, Ding YS, Wang GJ, Alexoff D: **A strategy for removing the bias in the graphical analysis method.** *J Cereb Blood Flow Metab* 2001, **21**:307–320.
19. Blomquist G, Englar H, Nordberg A, Ringheim A, Wall A, Forsberg A, Estrada M, Franberg P, Antoni G, Langstrom B: **Unidirectional influx and net accumulation of PIB.** *Open Neuroimag J* 2008, **2**:114–125.

doi:10.1186/2191-219X-3-76
Cite this article as: Sato *et al.*: Noninvasive k_3 estimation method for slow dissociation PET ligands: application to [^{11}C]Pittsburgh compound B. *EJNMMI Research* 2013 3:76.

Eur J Nucl Med Mol Imaging
DOI 10.1007/s00259-013-2620-7

ORIGINAL ARTICLE

Imaging of amyloid deposition in human brain using positron emission tomography and [^{18}F]FACT: comparison with [^{11}C] PIB

Hiroshi Ito · Hitoshi Shinotoh · Hitoshi Shimada · Michie Miyoshi · Kazuhiko Yanai · Nobuyuki Okamura · Harumasa Takano · Hidehiko Takahashi · Ryosuke Arakawa · Fumitoshi Kodaka · Maiko Ono · Yoko Eguchi · Makoto Higuchi · Toshimitsu Fukumura · Tetsuya Suhara

Received: 14 August 2013 / Accepted: 18 October 2013

Abstract
Purpose The characteristic neuropathological changes in Alzheimer's disease (AD) are deposition of amyloid senile plaques and neurofibrillary tangles. The ^{18}F-labeled amyloid tracer, [^{18}F]2-[(2-{(E)-2-[2-(dimethylamino)-1,3-thiazol-5-yl]vinyl}-1,3-benzoxazol-6-yl)oxy]-3-fluoropropan-1-ol (FACT), one of the benzoxazole derivatives, was recently developed. In the present study, deposition of amyloid senile plaques was measured by positron emission tomography (PET) with both [^{11}C]Pittsburgh compound B (PIB) and [^{18}F]FACT in the same subjects, and the regional uptakes of both radiotracers were directly compared.
Methods Two PET scans, one of each with [^{11}C]PIB and [^{18}F]FACT, were performed sequentially on six normal control subjects, two mild cognitive impairment (MCI) patients, and six AD patients. The standardized uptake value ratio of brain regions to the cerebellum was calculated with partial volume correction using magnetic resonance (MR) images to remove the effects of white matter accumulation.
Results No significant differences in the cerebral cortical uptake were observed between normal control subjects and AD patients in [^{18}F]FACT studies without partial volume correction, while significant differences were observed in [^{11}C]PIB. After partial volume correction, the cerebral cortical uptake was significantly larger in AD patients than in normal control subjects for [^{18}F]FACT studies as well as [^{11}C]PIB. Relatively lower uptakes of [^{11}C]PIB in distribution were observed in the medial side of the temporal cortex and in the occipital cortex as compared with [^{18}F]FACT. Relatively higher uptake of [^{11}C]PIB in distribution was observed in the frontal and parietal cortices.
Conclusion Since [^{18}F]FACT might bind more preferentially to dense-cored amyloid deposition, regional differences in cerebral cortical uptake between [^{11}C]PIB and [^{18}F]FACT might be due to differences in regional distribution between diffuse and dense-cored amyloid plaque shown in the autoradiographic and histochemical assays of postmortem AD brain sections.

Keywords Amyloid · Alzheimer · PET · FACT · PIB

H. Ito · H. Shinotoh · H. Shimada · M. Miyoshi · H. Takano · H. Takahashi · R. Arakawa · F. Kodaka · M. Ono · Y. Eguchi · M. Higuchi · T. Fukumura · T. Suhara
Molecular Imaging Center, National Institute of Radiological Sciences, Chiba, Japan

K. Yanai · N. Okamura
Department of Pharmacology, Tohoku University School of Medicine, Sendai, Japan

H. Ito (✉)
Biophysics Program, Molecular Imaging Center, National Institute of Radiological Sciences, 4-9-1 Anagawa, Inage-ku, Chiba 263-8555, Japan
e-mail: hito@nirs.go.jp

Published online: 14 November 2013

Introduction

Alzheimer's disease (AD) is the most common neurodegenerative dementia, and the characteristic neuropathological